OPEN ACCESS



A Titov–Démoulin Type Eruptive Event Generator for $\beta > 0$ Plasmas

Igor V. Sokolov and Tamas I Gombosi

Department of Climate and Space Sciences and Engineering University of Michigan, Ann Arbor, MI 48109, USA; igorsok@umich.edu
Received 2022 December 29; revised 2023 August 5; accepted 2023 August 8; published 2023 September 26

Abstract

We provide exact analytical solutions for the magnetic field produced by prescribed current distributions located inside a toroidal filament of finite thickness. The solutions are expressed in terms of toroidal functions, which are modifications of the Legendre functions. In application to the MHD equilibrium of a twisted toroidal current loop in the solar corona, the Grad–Shafranov equation is decomposed into an analytic solution describing an equilibrium configuration against the pinch-effect from its own current and an approximate solution for an external strapping field to balance the hoop force. Our solutions can be employed in numerical simulations of coronal mass ejections (CMEs). When superimposed on the background solar coronal magnetic field, the excess magnetic energy of the twisted current loop configuration can be made unstable by applying flux cancellation to reduce the strapping field. Such loss of stability accompanied by the formation of an expanding flux rope is typical for the Titov & Démoulin eruptive event generator. The main new features of the proposed model are as follows: the filament is filled with finite β plasma with finite mass and energy, the model describes an equilibrium solution that will spontaneously erupt due to magnetic reconnection of the strapping magnetic field arcade, and there are analytic expressions connecting the model parameters to the asymptotic velocity and total mass of the resulting CME, providing a way to connect the simulated CME properties to multipoint coronograph observations.

Unified Astronomy Thesaurus concepts: Magnetohydrodynamics (1964); Solar coronal mass ejections (310); Solar active region magnetic fields (1975)

Supporting material: animation

1. Introduction

Solar eruptions, including coronal mass ejections (CMEs), are associated with a major restructuring of the coronal magnetic field and the ejection of solar material ($\sim 10^{12}-10^{13}$ kg) and magnetic flux ($\sim 10^{13}-10^{15}$ Wb) into interplanetary space (e.g., Roussev & Sokolov 2006). Among many aspects of CMEs that justify the heliophysics community's interest in numerical simulations of CMEs is their contribution to the acceleration of solar energetic particles (SEPs). To explain the observed signatures of CME-SEP events, global models of solar eruptions need to incorporate the realistic background solution for the solar corona (SC) and magnetic field driven by observed magnetograms (see Roussev et al. 2004).

The fundamental process producing a CME is the conversion of magnetic free energy to the kinetic energy of the ejecta; that is why magnetically driven CME models are the most promising. A simple, but well working, way to drive a CME in a global simulation is to superimpose a Gibson & Low (1998; GL) or Titov & Démoulin (1999; TD) magnetic flux-tube configuration onto the background state of SC. These magnetic configurations describe an erupting magnetic filament. That filament becomes an expanding flux rope (magnetic cloud) in the ambient solar wind while evolving and propagating outward from the Sun, thus allowing the simulation of the propagation of a magnetically driven CME.

Our recent work on the GL model allowed us to significantly simplify the process of triggering CMEs. The product of the effort is the Eruptive Event Generator based on Gibson-Low

Original content from this work may be used under the terms of the Creative Commons Attribution 4.0 licence. Any further distribution of this work must maintain attribution to the author(s) and the title of the work, journal citation and DOI.

magnetic configuration (Jin et al. 2017), which is described in more details in Borovikov et al. (2017) in terms of an analytical solution of the Grad-Shafranov (GS; Grad & Rubin 1958; Shafranov 1966) equation. While the GL model represents significant progress in physics-based CME initiation modeling, it also has important limitations. When superimposed on the external field of the active region, the GL flux rope is already out of equilibrium, and it is expanding in a self-similar manner; therefore, it sidesteps the CME initiation problem. More importantly, the analysis based on the GS equation in Borovikov et al. (2017) demonstrated that the GL flux rope has regions of negative plasma β (the ratio of thermal to magnetic pressures), a clearly unphysical regime. The TD model inserts a toroidal loop (filament) carrying an electric current, I^{tot}, on top of the active region in a way that only part of the current loop is above the photosphere. The superposed magnetic configuration is stabilized by the effect of a strapping magnetic field, $B^{(s)}$ in the active region, such that the action of this field on the loop current, $\propto I^{\text{tot}} B^{(s)}$, balances the hoop force, $\propto (I^{\text{tot}})^2$ (see Titov et al. 2014), which allows for derivation of the current, I^{tot} , in terms of the observed magnetic field in the active region. If the equilibrium breaks, the filament immediately starts to expand, initiating an eruption. Recently, the model was generalized for inserting nontoroidal current loops by Titov et al. (2021), as well as for producing near-critical current loops using a helicity pumping method by Titov et al. (2022). The force-free TD model also has its own important limitation: the assumption of no mass (pressure) inside the filament is part of the equilibrium analysis ($\beta = 0$).

In spite of its limitations, the original TD flux rope model has been used in a number of studies (e.g., Roussev et al. 2003; Manchester et al. 2008, 2012; Jin et al. 2013). Starting with the work of Linker et al. 2016 and Török et al. 2018, numerous

impressive results were obtained with the modified TD configuration (Titov et al. 2014), simulating historic CME events with unprecedented clarity and completeness.

In this paper we describe an alternative TD approach, which addresses significant limitations of the Titov & Démoulin (1999) and Titov et al. (2014) models: our equilibrium analysis of the filament superposed with the potential field of the active region allows for finite mass and pressure ($\beta > 0$) inside the filament.

Similarly to the approach by Borovikov et al. (2017), this work is based on an analytical solution of the scalar GS equation. With the GS equation, one can describe a toroidal filament of twisted magnetic field lines filled with finite density plasma (ejecta). The solutions are expressed in terms of toroidal functions (see Appendix), which are straightforward modifications of Legendre functions.

We will apply this method to describe a twisted toroidal current loop in the SC that is in MHD equilibrium. In order to combine this filament with the active region magnetic field, an external strapping field must be accounted for in the force balance that balances the hoop force and thus assures equilibrium. We provide an approximate analytic solution to describe this combined configuration.

Note about notations.—This paper is highly mathematical, and some of the notations are easy to confuse. Here we briefly summarize our guiding philosophy concerning notations.

In general (dimensional), physical quantities described by functions of cylindrical coordinates z, r will be denoted by upper case letters:

- 1. J(z, r)—current density,
- 2. $\Psi(z, r)$ —flux function,
- 3. P(z, r)—gas-kinetic pressure.

Ouantities denoted by lower-case letters are reduced functions (or representative functions) of toroidal coordinates, u, v:

- 1. $\Psi(z, r) = \mu_0 \sqrt{R_{\infty} r} \ \psi(u.v),$
- 2. $J_{\varphi}(z, r) = \sqrt{R_{\infty}/r^5} j(u, v),$
- 3. $P(z, r) = (R_{\infty}/r)^3 p(u, v),$
- 4. $B_{\omega}(z, r) = (R_{\infty}/r)^{\frac{3}{2}} b(u, v)$.

Finally, quantities denoted with a "~" symbol represent normalized (dimensionless) quantities:

- 1. $\tilde{I}_n(u) = I_n(u)/I_{n_0}$,
- 2. $\tilde{j}_n = j_n/I_{n_0}$ 3. $\tilde{\psi}_n = \psi_n/I_{n_0}$.

2. Magnetostatics in Toroidal Coordinates

Equilibrium confinement of a toroidal plasma filament with a finite gas-kinetic pressure is controlled by a steady-state toroidal electric current, which produces an axially symmetric magnetic field that is independent of the toroidal angle, φ . The magnetostatics of such fields can be formulated in arbitrary orthogonal coordinates, $(u(r, z), v(r, z), \varphi)$. The meridional plane coordinates, (u, v), may or may not differ from cylindrical ones, (r, z), r being the distance from the axis of

In the 3D vector of magnetic field, $\mathbf{B} = \mathbf{B}_2 + B_{\varphi} \mathbf{e}_{\varphi}$, the poloidal components in the (z, r) plane, B_2 , can be expressed via the toroidal component of a vector potential, A_{φ} , using the Lamé coefficients, h_u , h_v (which describe the length element in

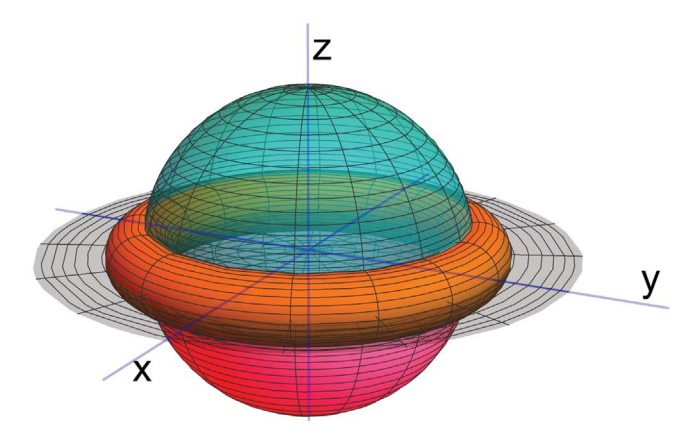


Figure 1. Toroidal coordinate surfaces for $R_{\infty}=1$: $\sinh u=5$ ($\kappa'\approx 0.1$)—orange torus; $\nu=0$ —gray part of plane z=0; $\nu=\pi/2$ —blue hemisphere; $v = \pi$ -invisible part of plane z = 0; $v = 3\pi/2$ —red hemisphere. Coordinate udecreases outward from the torus and increases inward, turning to infinity at the (invisible) circumference, $x^2 + y^2 = 1$, z = 0.

terms of infinitesimal $ds^2 = h_u^2 du^2 + h_v^2 dv^2 + r^2 d\varphi^2$): coordinate increments:

$$\mathbf{B}_2 = \frac{\nabla_2 \Psi}{r} \times \mathbf{e}_{\varphi},\tag{1}$$

where the 2D differential operator,

$$\nabla_2 \Psi = \frac{1}{h_u} \frac{\partial \Psi}{\partial u} \boldsymbol{e}_u + \frac{1}{h_v} \frac{\partial \Psi}{\partial v} \boldsymbol{e}_v, \tag{2}$$

is applied to the flux function, $\Psi = rA_{\phi}$. Instead of the full flux function, we will use (everywhere except Section 5.1) the "reduced" flux function, $\psi(u, v)$, that is defined in u, vcoordinates:

$$\Psi(z, r) = \mu_0 \sqrt{R_{\infty} r} \ \psi(u, v), \tag{3}$$

where R_{∞} is a characteristic scale to be specified later. Using Ampère's law, $\nabla_2 \times \mathbf{B}_2 = \mu_0 J_{\varphi} \mathbf{e}_{\varphi}$, in u, v coordinates, the expression for the toroidal current density, J_{ω} , can be simplified with the reduced flux function:

$$J_{\varphi}(z, r) = \sqrt{\frac{R_{\infty}}{r}} \frac{j(u, v)}{r^{2}},$$

$$j = \frac{3\psi}{4} - \frac{r^{2}}{h_{u}h_{v}} \left[\frac{\partial}{\partial u} \left(\frac{h_{v}}{h_{u}} \frac{\partial \psi}{\partial u} \right) + \frac{\partial}{\partial v} \left(\frac{h_{u}}{h_{v}} \frac{\partial \psi}{\partial v} \right) \right], \tag{4}$$

where we introduced a representative function for the toroidal current density, j(u, v), that only depends on the generalized coordinates.

Next, we define the toroidal coordinates in the meridional plane (u, v) in the following way (see Morse & Feshbach 1953, and Figure 1):

$$r = \frac{R_{\infty} \sinh u}{\cosh u - \cos v}, \qquad z = \frac{R_{\infty} \sin v}{\cosh u - \cos v},$$

$$h_u = h_v = \frac{R_{\infty}}{\cosh u - \cos v} = \frac{r}{\sinh u}.$$
 (5)

From these definitions, we get the following relation for the normalized radius vector to the (r, z) point:

$$\left(\frac{r}{R_{\infty}}\right)^{2} + \left(\frac{z}{R_{\infty}}\right)^{2} = \frac{\cosh u + \cos v}{\cosh u - \cos v}$$
$$= 1 + \frac{2z}{R_{\infty}}\cot v = -1 + \frac{2r}{R_{\infty}}\coth u. \tag{6}$$

This means that surfaces of constant $v=v_0$ are spheres with centers at r=0, $z=R_{\infty}\cot v_0$, and radii of $R_{\infty}/|\sin v_0|$. Surfaces of constant $u=u_0$ are tori with major radii $R_{\infty}\coth u_0$ and minor radii $R_{\infty}/\sinh u_0$. Specifically, when $u\to\infty$, the major and minor radii become R_{∞} and 0, respectively. This is a degenerated toroidal surface of zero minor radius (toroidal magnetic axis).

The inverse transformations determine the toroidal coordinates, u, v, and the Lamé coefficients in terms of r, z:

$$\sin v = \frac{2R_{\infty}z}{R_{+}R_{-}}, \qquad \cos v = \frac{R^{2} - R_{\infty}^{2}}{R_{+}R_{-}},$$

$$\sinh u = \frac{2R_{\infty}r}{R_{+}R_{-}}, \qquad h_{u,v} = \frac{R_{+}R_{-}}{2R_{\infty}}, \qquad (7)$$

where $R = \sqrt{\mathbf{R}^2}$, $\mathbf{R} = r\mathbf{e}_r + z\mathbf{e}_z$ is the radius vector pointing from the center, and z = 0, r = 0 to a given point,

$$R_{\pm} = \sqrt{(r \pm R_{\infty})^2 + z^2},$$
 (8)

are the maximum (+) and minimum (-) distances from the given point to the toroidal magnetic axis.

The magnetic field can be expressed in terms of *toroidal* special functions of the toroidal coordinate, u. Note, that the presence of u, u_0 in the equations is quite formal, and they are not actually calculated, since in effect the special functions can be expressed and efficiently calculated as hypergeometric power series of either $\kappa(u)$ or $\kappa'(u)$, which can in turn be expressed in terms of R_+ :

$$\kappa^{2}(u) = 1 - e^{-2u} = \frac{4R_{\infty}r}{R_{+}^{2}},$$

$$\kappa'(u) = \sqrt{1 - \kappa^{2}} = e^{-u} = \frac{R_{-}}{R_{+}}.$$
(9)

Using these notations, the toroidal coordinate surface, u= const, has minor radius, $a=2\kappa'R_\infty/(1-\kappa'^2)$, and major radius, $R_0=\sqrt{R_\infty^2+a^2}$, determined by the constant value of κ' , at the surface. Any such surface can be taken as the boundary of a toroidal current filament. Conversely, the field of a toroidal current filament with known minor and major radii of a, R_0 , can be described using toroidal coordinates with a characteristic length scale of $R_\infty=\sqrt{R_0^2-a^2}$, so that the filament boundary is a $u=u_0=$ const surface at which $\kappa'_0=\kappa'(u_0)=a/(R_0+R_\infty)$. This surface separates the filament interior $(u_0\leqslant u<\infty)$ from its exterior $(0< u< u_0)$. Note, that for $u\to 0$ $\lim_{u\to 0} \kappa=0$, while for $u\to\infty$ (at the toroidal magnetic axis) $\lim_{u\to\infty}\kappa'=0$.

The coordinate unit vectors are as follows:

$$\mathbf{e}_{v} = \frac{(R^{2} - R_{\infty}^{2})\mathbf{e}_{z} - 2\mathbf{R}(\mathbf{R} \cdot \mathbf{e}_{z})}{R_{-}R_{+}}$$

$$\equiv \frac{(\cosh u \cos v - 1)\mathbf{e}_{z} - \sinh u \sin v \mathbf{e}_{r}}{\cosh u - \cos v}, \tag{10}$$

$$\mathbf{e}_{u} = [\mathbf{e}_{v} \times \mathbf{e}_{\varphi}]$$

$$= \frac{-\sinh u \sin v \ \mathbf{e}_{z} - (\cosh u \cos v - 1)\mathbf{e}_{r}}{\cosh u - \cos v}.$$
(11)

With the help of the Lamé coefficients (Equation (5)), one can express the (poloidal) magnetic field (Equation (1)),

$$\boldsymbol{B}_{2} = \frac{\mu_{0} R_{\infty}^{\frac{1}{2}}}{2r^{\frac{3}{2}}} \left[\psi \boldsymbol{e}_{z} + \frac{\kappa^{2}}{\kappa'} \left(\frac{\partial \psi}{\partial v} \boldsymbol{e}_{u} - \frac{\partial \psi}{\partial u} \boldsymbol{e}_{v} \right) \right], \tag{12}$$

and the toroidal current density (Equation (4)):

$$j = \sinh^2 u \left[-\frac{\partial^2 \psi}{\partial u^2} - \frac{\partial^2 \psi}{\partial v^2} + \frac{3\psi}{4 \sinh^2 u} \right]. \tag{13}$$

Any solution of scalar Equation (13) that relates the form factor of the toroidal current to the reduced flux function, allows for expressing the vector poloidal magnetic field via Equation (12). In particular, we will present manufactured solutions, which, for some special choices of the current form factor, lead to analytic expressions for the magnetic field.

3. Deriving the Reduced Flux Function with the Fourier Method

Equation (13) can be solved because the Laplacian in toroidal coordinates allows for the separation of variables within the framework of the Fourier method. Both currents and fields are expressed in terms of products of eigenfunctions of a single variable depending either on u or on v. This way, a variety of solutions can be derived expressing the field analytically in terms of special toroidal functions. Indeed, the scalar function appearing in the poloidal magnetic field (see Equation (12)) can be expressed as a complex series:

$$\psi = \sum_{n=-\infty}^{\infty} e^{inv} \psi_n(u), \quad \psi_n = \psi_{-n}^*, \tag{14}$$

where $i^2 = -1$, and the superscript asterisk means complex conjugation.

To find the magnetic field harmonics, the current, j(u, v), in Equation (4) is also expanded into a Fourier series:

$$j(u, v) = \sum_{n = -\infty}^{\infty} e^{inv} j_n(u), \qquad j_n = j_{-n}^*.$$
 (15)

Equations relating the magnetic field and current harmonics can be derived from Equations (13), (14), and (15) as follows:

$$-\frac{d^2\psi_n}{du^2} + \left(n^2 + \frac{3}{4\sinh^2 u}\right)\psi_n = \frac{j_n(u)}{\sinh^2 u}.$$
 (16)

The substitution, $\psi_n = \sqrt{2 \sinh u} \, \mathcal{P}_n(u)$, reduces this equation with zero on the right-hand side (RHS) to the equation for Legendre functions of semi-integer index, $P_{n-\frac{1}{2}}^{-1}(\cosh u)$ and

 $Q_{n-\frac{1}{2}}^{-1}(\cosh u)$. The eigenfunctions of Equation (16) are

$$\bar{P}_{n-\frac{1}{2}}^{-1}(u) = \sqrt{2} \sinh u \, P_{n-\frac{1}{2}}^{-1}(\cosh u),$$

$$\bar{Q}_{n-\frac{1}{2}}^{-1}(u) = \sqrt{2} \sinh u \, Q_{n-\frac{1}{2}}^{-1}(\cosh u),$$
(17)

(see Equations (A2) and (A7)), which are referred to as *toroidal* functions. Since the toroidal current is assumed to vanish outside the torus, i.e., $J_{\varphi} = 0$ for $0 < u < u_0$, the field in this region can be expressed as a series of toroidal functions of the first kind: $\psi_n \propto \bar{P}_{n-\frac{1}{2}}^{-1}(u)$, because the Legendre functions of the

second kind, $\bar{Q}_{n-\frac{1}{2}}^{-1}(u)$, are singular at $u \to 0$.

The current, I(u), through a contour of constant u, can be expressed as a series of harmonics:

$$I(u) = \int_{u}^{\infty} \int_{0}^{2\pi} J_{\varphi} h_{u} h_{v} \, dv du_{1} = \sum_{n=-\infty}^{\infty} I_{n}(u),$$

$$I_{n}(u) = \int_{u}^{\infty} \left(\int_{0}^{2\pi} e^{inv} \sqrt{\frac{R_{\infty}}{r}} \, dv \right) \frac{j_{n}(u_{1})}{\sinh^{2} u_{1}} du_{1}$$
(18)

where the inner integral over v can be evaluated using Equation (A14), yielding:

$$I_n(u) = \int_u^\infty \bar{Q}_{n-\frac{1}{2}}^{-1}(u_1) \frac{j_n(u_1)}{\sinh^2 u_1} du_1.$$
 (19)

The *n*th harmonics of the total current through the current loop, $I_n(u_0)$, will be denoted as I_{n_0} :

$$I^{\text{tot}} = \sum_{n = -\infty}^{\infty} I_{n_0} = \sum_{n = -\infty}^{\infty} I_n(u_0).$$
 (20)

Similarly, with the help of Equation (A15), the harmonics of magnetic moment defined as the volume integral, $\mathcal{M} = \frac{1}{2} \int r J_{\varphi} dV$, can be obtained in terms of quantities introduced above:

$$\mathcal{M} = \pi \int_{u_0}^{\infty} \int_{0}^{2\pi} J_{\varphi} r^{2} h_{u} h_{v} \, dv du_{1}$$

$$= \pi R_{\infty}^{2} \int_{u}^{\infty} \left(\int_{0}^{2\pi} e^{inv} \sqrt{\frac{r^{3}}{R_{\infty}^{3}}} \, dv \right) \frac{j_{n}(u_{1})}{\sinh^{2} u_{1}} du_{1}$$

$$= \pi R_{\infty}^{2} \sum_{n=-\infty}^{\infty} (1 - 4n^{2}) I_{n_{0}}.$$
(21)

The quantities, $I_n(u)$, $j_n(u)$, as well as $\psi_n(u)$ all have dimensions of current; therefore, it is convenient to characterize the distributions of current and reduced flux function with the dimensionless quantities normalized by the appropriate harmonics of total current:

$$\tilde{I}_{n}(u) = \frac{I_{n}(u)}{I_{n_{0}}}, \quad \tilde{I}_{n}(u_{0}) = 1,
\tilde{J}_{n}(u) = \frac{j_{n}(u)}{I_{n_{0}}}, \quad \int_{u_{0}}^{\infty} \bar{Q}_{n-\frac{1}{2}}^{-1}(u_{1}) \frac{\tilde{J}_{n}(u_{1})}{\sinh^{2}u_{1}} du_{1} = 1,
\tilde{\psi}_{n}(u) = \frac{\psi_{n}(u)}{I_{n_{0}}}.$$
(22)

One can express the magnetic field harmonics in terms of the current harmonics using a convolution integral (see

Equation (A12)):

$$\tilde{\psi}_n = \int_{u_0}^{\infty} G_n(u, u_1) \frac{\tilde{j}_n(u_1)}{\sinh^2 u_1} du_1$$
 (23)

where we introduced the Green function,

$$G_n(u, u_1) = \left(\frac{1}{8} - \frac{n^2}{2}\right) \bar{P}_{n-\frac{1}{2}}^{-1}(\min(u, u_1))$$

$$\times \bar{Q}_{n-\frac{1}{3}}^{-1}(\max(u, u_1)). \tag{24}$$

Following general rules, the Green function is constructed from the eigenfunctions of Equation (16) satisfying the proper boundary conditions. While it is continuous, its derivative, $\partial G_n/\partial u=1$, has a discontinuity at $u=u_1$ in a way that the second derivative equals the negative of the Dirac δ -function. This is why Equation (23) provides a solution to Equation (16) for a given current on the RHS.

Inside the current filament, $(u > u_0)$, the integration of the Green function (Equation (24)) gives:

$$\tilde{\psi}_{n}(u > u_{0}) = \left(\frac{1}{8} - \frac{n^{2}}{2}\right) [\bar{P}_{n-\frac{1}{2}}^{-1}(u)\tilde{I}_{n}(u)
+ \bar{Q}_{n-\frac{1}{2}}^{-1}(u) \int_{u_{0}}^{u} \frac{\bar{P}_{n-\frac{1}{2}}^{-1}(u_{1})\tilde{J}_{n}(u_{1})du_{1}}{\sinh^{2}u_{1}} \right].$$
(25)

Outside the current loop where $u \le u_0 \le u_1$, Equations (23) and (24) give:

$$\tilde{\psi}_n(u \leqslant u_0) = \left(\frac{1}{8} - \frac{n^2}{2}\right) \bar{P}_{n-\frac{1}{2}}^{-1}(u). \tag{26}$$

Even though the reduced flux functions in Equations (25) and (26) are continuous at the filament surface ($u = u_0$), the derivatives might be discontinuous when the finite surface current is concentrated at the filament boundary.

To conclude this Section, we provide an equation for the total reduced flux function for the case when the current distribution is symmetric with respect to the z=0 plane, so that the flux is an even function of v, the current amplitudes are real functions, and one can use $e^{inv} \equiv \cos(nv)$. With these simplifications, the reduced flux function becomes (see Equations (14) and (26)):

$$\psi(u \leqslant u_0) = \sum_{n=-\infty}^{\infty} \left(\frac{1}{8} - \frac{n^2}{2}\right) I_{n_0} \bar{P}_{n-\frac{1}{2}}^{-1}(u) \cos(nv),$$

$$I_{n_0} = I_{-n_0}.$$
(27)

We can also provide the Fourier series for the external field of the same symmetry. The currents producing this field are all located outside the filament, and there is no singularity at the toroidal magnetic axis; hence, inside the filament, the expansion for this field is as follows:

$$\psi^{(\text{ext})}(u \geqslant u_0) = \sum_{n=-\infty}^{\infty} \psi_n^{(\text{ext})} \bar{Q}_{n-\frac{1}{2}}^{-1}(u) \cos(nv),$$

$$\psi_n^{(\text{ext})} = \psi_{-n}^{(\text{ext})}.$$
(28)

Note that the sum of the self-generated and external magnetic fields vanishes at the filament boundary, $\psi(u=u_0)+\psi^{(\text{ext})}(u=u_0)\equiv 0$, for the following specific choice

of the external field harmonic amplitudes:

$$\psi_n^{\text{(ext)}} = -\ell_n^{\text{(s)}}(u_0)I_{n_0},\tag{29}$$

$$\ell_n^{(s)}(u_0) = \left(\frac{1}{8} - \frac{n^2}{2}\right) \frac{\bar{P}_{n-\frac{1}{2}}^{-1}(u_0)}{\bar{Q}_{n-\frac{1}{2}}^{-1}(u_0)}.$$
 (30)

Hereafter, $\ell_n^{(s)}(u_0)$ are the dimensionless induction coefficients (proportional to the flux-to-current ratios), which are—as demonstrated below (see Section 5.5)—closely related to the energy of the external poloidal magnetic field produced by the current filament. The capability of the external field given by Equations (28) and (29) to turn the plasma boundary to a magnetic surface (at which $\Psi = \text{const}$) is discussed in Section 5.1 below.

4. Constructing Magnetic Field Configurations for the Zeroth Harmonic

Our objective is to construct simple, analytic expressions for a twisted toroidal magnetic flux rope that can be superimposed on observed solar active region magnetic fields. Such a configuration can be obtained using the lowest-order harmonics of the Fourier series solution discussed in Section 3.

Let us assume that there is only the n=0 Fourier harmonic in the current distribution, $\tilde{f}(u) \equiv \tilde{f}_0(u)$, which only depends on u. The subscript "0" that denotes quantities related to the n=0 harmonic is omitted herewith. The only contribution to the total current comes from this harmonic, $I^{\text{tot}} = I_{0_0} = I_0(u_0)$. Now, we consider the n=0 harmonic of the magnetic field, in which the reduced flux function, $\tilde{\psi} \equiv \tilde{\psi}_0(u)$, also only depends on u, so that Equation (12) becomes:

$$\boldsymbol{B}_0 = B_c \left(\frac{R_\infty}{r}\right)^{\frac{3}{2}} [B^{(z)}(u)\boldsymbol{e}_z - B^{(p)}(u)\boldsymbol{e}_v], \tag{31}$$

where

$$B_c = \frac{\mu_0 I^{\text{tot}}}{2R_{20}},\tag{32}$$

is the magnetic field at the origin, R = 0. The dimensionless amplitudes,

$$B^{(z)}(u) \equiv \tilde{\psi}, \quad B^{(p)}(u) \equiv \frac{\kappa^2}{\kappa'} \frac{d\tilde{\psi}}{du},$$
 (33)

describe the axial and poloidal fields, respectively. It is convenient to eliminate the false singularity in e_{ν} , by transforming the denominator in Equation (10) using the definitions of R_{\pm} and κ' (Equations (8) and (9)): $R_{-}R_{+} = \kappa' R_{+}^{2}$, so that Equation (31) can be written as:

$$\boldsymbol{B}_{0} = \left(\frac{R_{\infty}}{r}\right)^{\frac{3}{2}} B_{c} \left[B^{(z)}(u)\boldsymbol{e}_{z} - \frac{B^{(p)}(u)}{\kappa'}(\kappa'\boldsymbol{e}_{v})\right], \tag{34}$$

where the singularity is eliminated:

$$(\kappa' \boldsymbol{e}_{v}) = \frac{(R^{2} - R_{\infty}^{2})\boldsymbol{e}_{z} - 2\boldsymbol{R}(\boldsymbol{R} \cdot \boldsymbol{e}_{z})}{R^{2}}.$$
 (35)

In order to eliminate another false singularity in Equation (34) *outside* the torus ($u < u_0$), we use the definition

of κ given by Equation (9):

$$\left(\frac{R_{\infty}}{r}\right)^{\frac{3}{2}} = \frac{8R_{\infty}^3}{\kappa^3 R_{\infty}^3}.\tag{36}$$

Substituting this expression into Equation (34) yields

$$\boldsymbol{B}_{0} = \frac{8R_{\infty}^{3}}{R_{+}^{3}} B_{c} \left[\frac{B^{(z)}(u)}{\kappa^{3}} \boldsymbol{e}_{z} - \frac{B^{(p)}(u)}{\kappa^{3} \kappa'} (\kappa' \boldsymbol{e}_{v}) \right]. \tag{37}$$

For n = 0 the field amplitude and its derivative appearing in Equation (33) can be obtained outside the filament from the reduced flux function, Equation (26):

$$\tilde{\psi}(u \leqslant u_0) = \frac{1}{8} \bar{P}_{-\frac{1}{2}}^{-1}(u),$$

$$\frac{\kappa^2}{\kappa'} \frac{\tilde{\psi}(u \leqslant u_0)}{du} = \frac{3}{8} \bar{P}_{\frac{1}{2}}^{-1}(u),$$
(38)

so that Equation (37) reads:

$$\mathbf{B}_{0}(u \leqslant u_{0}) = \frac{R_{\infty}^{3}}{R_{+}^{3}} B_{c}$$

$$\times \left\{ \left[\frac{\bar{P}_{-\frac{1}{2}}^{-1}(u)}{\kappa^{3}} \right] \mathbf{e}_{z} - 3 \left[\frac{\bar{P}_{\frac{1}{2}}^{-1}(u)}{\kappa^{3} \kappa'} \right] (\kappa' \mathbf{e}_{v}) \right\}. \tag{39}$$

The ratio, $\bar{P}_{n-\frac{1}{2}}^{-1}(u)/[\kappa^3(\kappa')^n]$, that appears twice in Equation (39) can be expressed in terms of a hypergeometric series of powers of κ^2 (see Equation (A2)). For $\kappa \to 0$ it approaches 1/4. Specifically, at the center where, according to Equations (8), (9), and (10), $\kappa = 0$, R = 0, $R_+ = R_\infty$, and $(\kappa' e_v) \to -e_z$, this approximation of the toroidal functions in Equation (39) gives $\lim_{R\to 0} \mathbf{B}_0 = \mathbf{B}_c \mathbf{e}_z$, as required.

At large distances from the filament, $R \gg R_{\infty}$, Equation (39) approaches the magnetic field of a dipole with the magnetic moment of the n=0 harmonic given by Equation (21):

$$\mathcal{M} = \pi R_{\infty}^2 I^{\text{tot}} \mathbf{e}_{\tau}. \tag{40}$$

Close to the current loop, where $\kappa \approx 1$ and Equations (10) and (11) at $u \to \infty$ can be approximated as follows:

$$e_v \approx \cos v \ e_z - \sin v \ e_r,$$

 $e_u \approx -\sin v \ e_z - \cos v \ e_r,$ (41)

one can approximate functions $\bar{P}_{\pm\frac{1}{2}}^{-1}(u)$ using Equations (A6) and demonstrate that the external poloidal field dominates:

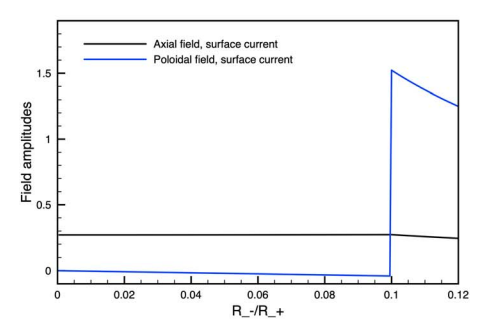
$$\boldsymbol{B}_0 \approx \frac{\mu_0 I^{\text{tot}}}{2\pi R_-} (\boldsymbol{e}_r \sin v - \boldsymbol{e}_z \cos v). \tag{42}$$

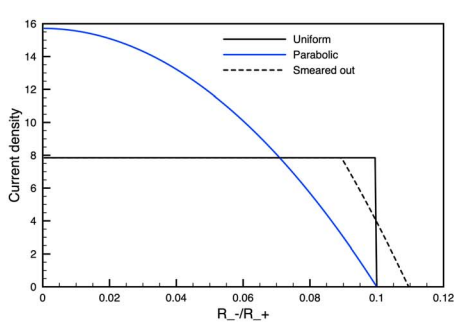
In effect, Equation (39), describes the magnetic field of an infinitely thin ring current with major radius of R_{∞} , even though it is derived as the magnetic field of an arbitrary *u*-dependent current distribution. Furthermore, it is not required that the ratio, a/R_0 , be small. In addition, the major radius of the current filament differs from that of the infinitely thin ring, $R_0 \neq R_{\infty}$.

A simple example for the field *inside* the filament can be found if the current is concentrated at the filament surface:

$$\tilde{\psi}(u \geqslant u_0) = \ell^{(s)}(u_0)\bar{Q}_{-\frac{1}{2}}^{-1}(u),$$

$$\frac{\kappa^2}{\kappa'}\frac{\tilde{\psi}(u \leqslant u_0)}{du} = 3\ell^{(s)}(u_0)\bar{Q}_{\frac{1}{2}}^{-1}(u),$$
(43)





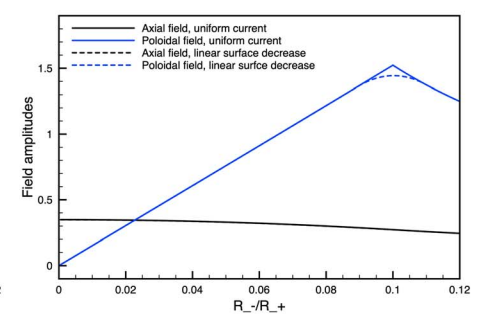


Figure 2. Left panel: amplitudes of poloidal (blue line) and axial (black line) magnetic field components for the current concentrated at the filament boundary. Middle panel: normalized current distributions for uniform (black solid line), parabolic (blue line), and linear surface decrease current (black dashed line) for $\varepsilon = 0.1$. Right panel: amplitudes of poloidal (blue line) and axial magnetic field (black line) components for uniform current (solid lines) and for linear surface decrease current (dashed lines). For $\kappa'_0 = 0.1$ ($a/R_0 \approx 0.2$) the argument, $\kappa' = R_-/R_+$, ranges from $\kappa' = 0$ (at the toroidal magnetic axis) to $\kappa' = 0.1$ at the filament boundary; while $\kappa' > 0.1$ values correspond to the loop exterior.

where

$$\ell^{(s)}(u_0) = \frac{\bar{P}_{-\frac{1}{2}}^{-1}(u_0)}{8\bar{Q}_{-\frac{1}{2}}^{-\frac{1}{2}}(u_0)}.$$
 (44)

Here $l^{(s)} = l_0^{(s)}$ is a dimensionless induction coefficient for n = 0 (see general definition in Equation (29)) proportional to the flux-to-current ratio for the surface current. Equations (38) and (43) can be combined and written in terms of the Green function, Equation (24):

$$\tilde{\psi} = \frac{G_0(u, u_0)}{\bar{Q}_{-\frac{1}{2}}^{-1}(u_0)}.$$
(45)

Below we consider several specific situations and express $\tilde{\psi}$ in terms of the Green function(s), while the field amplitudes, $B^{(z,p)}$, are expressed in terms of the normalized reduced flux function, $\tilde{\psi}$. The amplitudes of poloidal (blue line) and axial (black line) magnetic fields are shown in the left panel of Figure 2.

A variety of more realistic solutions for the magnetic field inside a plasma can be constructed by approximating the current profile as a linear combination of specially chosen current profiles ("form-factors"), $j^{(m)}$ with constant coefficients, c_m ,

$$j(u) = \sum_{m} c_m j^{(m)}(u).$$
 (46)

The specially chosen form-factors satisfy the equation:

$$\left(-\sinh^2 u \frac{d^2}{du^2} + \frac{3}{4}\right) j^{(m)} = E^{(m)} j^{(m)},$$

$$j^{(0)}(u) = 1, \quad j^{(1)}(u) = \coth u,...$$

$$E^{(0)} = \frac{3}{4}, \quad E^{(1)} = -\frac{5}{4},...$$
(47)

With this choice, the integral in Equation (19) can be evaluated analytically:

$$I(u) = \bar{Q}_{-\frac{1}{2}}^{-1}(u)\frac{dj_{E}(u)}{du} - j_{E}(u)\frac{d\bar{Q}_{-\frac{1}{2}}^{-1}(u)}{du},$$

$$j_{E}(u) = \sum_{m} \frac{c_{m}j_{0}^{(m)}(u)}{E^{(m)}},$$
(48)

(see Appendix A.4 for more details). Equation (48) provides a simple normalization recipe: (1) for a current profile given by Equation (46), the modified current distribution, $j_E(u)$, should be constructed according to Equation (48); (2) using $j_E(u)$ the normalization integral,

$$N = \bar{Q}_{-\frac{1}{2}}^{-1}(u_0)\frac{dj_E(u_0)}{du_0} - j_E(u_0)\frac{d\bar{Q}_{-\frac{1}{2}}^{-1}(u_0)}{du_0}$$
(49)

should be calculated; and (3) the normalized current distributions are calculated then as $\tilde{j}(u) = j(u)/N$ and $\tilde{j}_E(u) = j_E(u)/N$. The normalized current satisfies the identity:

$$\bar{Q}_{-\frac{1}{2}}^{-1}(u_0)\frac{d\tilde{j}_E(u_0)}{du_0} - \tilde{j}_E(u_0)\frac{d\bar{Q}_{-\frac{1}{2}}^{-1}(u_0)}{du_0} = 1.$$
 (50)

Specifically, for "uniform" current when j = const:

$$\tilde{j} = \frac{1}{N^{\text{uni}}(u_0)}, \quad \tilde{j}_E = \frac{1}{E^{(0)}N^{\text{uni}}(u_0)},
N^{\text{uni}}(u_0) = -\frac{1}{E^{(0)}} \frac{d\bar{Q}_{-\frac{1}{2}}^{-1}(u_0)}{du_0}.$$
(51)

For a "parabolic" current profile, we get:

$$\tilde{J} = \frac{\coth(u_0) - \coth u}{N^{\text{par}}(u_0, u_0)},
\tilde{J}_E = \frac{\coth(u_0)}{E^{(0)}N^{\text{par}}(u_0, u_0)} - \frac{\coth u}{E^{(1)}N^{\text{par}}(u_0)},
N^{\text{par}}(u_0, u) = \frac{\bar{Q}_{-\frac{1}{2}}^{-1}(u)}{E^{(1)}\sinh^2(u)}
- \left(\frac{\coth(u_0)}{E^{(0)}} - \frac{\coth(u)}{E^{(1)}}\right) \frac{d\bar{Q}_{-\frac{1}{2}}^{-1}(u)}{du}.$$
(52)

Even though a uniform current results in an even simpler solution, the discontinuous current profile near the filament boundary results in large numerical errors in various physical quantities. In order to eliminate this discontinuity, one can consider the current distribution given by Equation (46) with piecewise constant coefficients, c_m , combining the features of Equations (51) and (52) to "linearly" decrease the current density over a narrow interval of $u_0 - \varepsilon < u < u_0 + \varepsilon, \varepsilon \ll 1$. Specifically, we define the boundaries, (u_0^-, u_0^+) of this interval with the equation, $\kappa'(u_0^+) = \sqrt{1 \pm 2\varepsilon} \, \kappa'_0$. This leads to the

following expressions:

$$\tilde{j} = \begin{cases}
\frac{\coth u_0^- - \coth u}{[\coth(u_0^-) - \coth(u_0^+)] \Sigma N}, & \text{if } u_0^- < u < u_0^+ \\
\frac{1}{2N}, & \text{if } u > u_0^+, \\
\end{cases}$$

$$\tilde{j}_E = \begin{cases}
\frac{\frac{1}{E^{(0)}} \coth u_0^- - \frac{1}{E^{(1)}} \coth u}{[\coth(u_0^-) - \coth(u_0^+)] \Sigma N}, & \text{if } u_0^- < u < u_0^+ \\
\frac{1}{E^{(0)} \Sigma N}, & \text{if } u > u_0^+, \\
\end{cases}$$

$$\Sigma N = N^- + N^+, \quad N^- = \frac{N^{\text{par}}(u_0^-, u_0^-)}{\coth(u_0^-) - \coth(u_0^+)},$$

$$N^+ = -\frac{N^{\text{par}}(u_0^-, u_0^+)}{\coth(u_0^-) - \coth(u_0^+)} + N^{\text{uni}}(u_0^+).$$
(53)

In the case of a thin filament, these expressions give $\tilde{j} \approx 1/\pi a^2$ if $0 \le R_- \le (1-\varepsilon)a$, and $\tilde{j} \approx (1+\varepsilon)a - R_-/(2\pi\varepsilon a^3)$ if $(1-\varepsilon)a \le R_- \le (1+\varepsilon)a$. The normalized current density distributions given by Equations (51)–(53) are shown in Figure 2 (middle panel).

With the help of Equation (A12), one can evaluate the integral in Equation (25) for n = 0 (similarly to Equation (48)), to find the reduced flux function and then the field amplitudes:

$$\tilde{\psi} = \frac{G_0(u, u_0)}{\bar{Q}_{-\frac{1}{2}}^{-1}(u_0)}
+ \begin{cases}
0, & \text{if } u < u_0 \\
\tilde{j}_E(u) - \frac{\tilde{j}_E(u_0)\bar{Q}_{-\frac{1}{2}}^{-1}(u)}{\bar{Q}_{-\frac{1}{2}}^{-1}(u_0)}, & \text{if } u > u_0,
\end{cases} (54)$$

This result is easy to verify and interpret: (1) by applying the differential operator on the left-hand side (LHS) of Equation (16) to Equation (54) and taking into account Equation (47), one can see that Equation (16) is satisfied in smooth regions; (2) the reduced flux function Equation (54) is continuous; and (3) the jump in the derivative of the second term at $u = u_0$ is canceled by the controlled jump in the derivative of the Green function (see the discussion above), as it follows from Equations (50) and (A12). In the special case of constant form factor given by Equation (51), we get:

$$\tilde{j}_E(u) \equiv -\left(\frac{d\bar{Q}_{-\frac{1}{2}}^{-1}(u_0)}{du_0}\right)^{-1}, \quad \frac{d\tilde{j}_E(u)}{du} \equiv 0.$$
 (55)

The amplitudes, $B^{(p)}(\kappa'(u))$ and $B^{(z)}(\kappa'(u))$, of the poloidal (solid curve) and axial (dashed curve) fields are shown in Figure 2 with black color. Outside the filament at $\kappa'(u) > \kappa'(u_0)$, the field does not depend on the current distribution; therefore, the black and blue curves overlap in this region. For the form-factor Equation (53), the integration span in Equations (19) and (25) splits for domains separated by u_0^+ , resulting in different expressions for the fields in these

domains:

$$\tilde{\psi} = \frac{N^{-}}{\Sigma N} \frac{G_{0}(u, u_{0}^{-})}{\bar{Q}_{-\frac{1}{2}}^{-1}(u_{0}^{-})} + \frac{N^{+}}{\Sigma N} \frac{G_{0}(u, u_{0}^{+})}{\bar{Q}_{-\frac{1}{2}}^{-1}(u_{0}^{+})}
+ \begin{cases}
0, & \text{if } u < u_{0}^{-} \\
\tilde{j}_{E}(u) - \frac{\tilde{j}_{E}(u_{0}^{-})\bar{Q}_{-\frac{1}{2}}^{-1}(u)}{\bar{Q}_{-\frac{1}{2}}^{-1}(u_{0}^{-})}, & \text{if } u_{0}^{-} < u, \end{cases}
+ \begin{cases}
0, & \text{if } u < u_{0}^{+} \\
\Delta[\tilde{j}_{E}(u_{0}^{+})] \frac{\bar{Q}_{-\frac{1}{2}}^{-1}(u)}{\bar{Q}_{-\frac{1}{2}}^{-1}(u_{0}^{+})}, & \text{if } u_{0}^{+} < u, \end{cases}$$
(56)

where $\Delta[\tilde{j}_E(u_0^+)] = \tilde{j}_E(u_0^+ - 0) - \tilde{j}_E(u_0^+ + 0)$ is the difference between the left and right limits of discontinuous function, \tilde{j}_E at $u \to u_0^+$ (in contrast with the continuous current density function, \tilde{j}).

Note that once Equations (34) and (39) are applied in the CME generator, their vector form allows us to calculate the field in any coordinate system without rotating the vector quantities to the system used in derivations presented in this paper. Indeed, these equations, together with Equation (35), express the magnetic field vector as a linear combination of vectors e_z and R; therefore, the expression is valid in any coordinate system as long as the vectors e_z and R are given in the same coordinate system.

Specifically, in an arbitrary Cartesian coordinate system it is convenient to characterize the position of the current filament by the coordinates of its center, R_c , and the unit vector, n_c , directed along its axis of symmetry. Then, the field vector at a point, R', is given by Equations (34), (35), and (39) with the following substitution:

$$\mathbf{R} = \mathbf{R}' - \mathbf{R}_c, \qquad \mathbf{e}_z = \mathbf{n}_c. \tag{57}$$

To calculate scalar functions, we also need to express:

$$z = (\mathbf{R}' - \mathbf{R}_c) \cdot \mathbf{n}_c, \quad R^2 = (\mathbf{R}' - \mathbf{R}_c)^2,$$

$$r = \sqrt{R^2 - z^2}, \quad R_{\pm} = \sqrt{(r \pm R_{\infty})^2 + z^2}.$$
 (58)

To calculate the toroidal special function in Equations (39) and (54) for field amplitudes, one can calculate their arguments κ and κ' , using Equations (9) and (58). While the formulae for the magnetic field are repeatedly applied at each point where the magnetic field is needed, the filament parameters, $R_{\infty} = \sqrt{R_0^2 - a^2}$, $\kappa'_0 = a/(R_{\infty} + R_0)$, $\kappa_0^2 = 1 - (\kappa'_0)^2$, and the coefficients $\tilde{j}_E(u_0)$, $q_1(u_0)$ (Equation (55)) determining the field amplitudes are calculated only once in terms of the major and minor radii, R_0 , a.

5. Equilibrium Conditions for the Zeroth Harmonic

5.1. Full Grad-Shafranov Equation in Cylindrical Coordinates

The MHD equilibrium theory of toroidal plasma configurations introduces the key concept of *magnetic surfaces*, where the flux function, Ψ , is constant. To apply this concept, let us start by expressing Equations (1) and (4) in cylindrical coordinates ($u \equiv z$, $v \equiv r$, $H_z = H_r \equiv 1$):

$$\mathbf{B}_{2} = \frac{\nabla_{2}\Psi}{r} \times \mathbf{e}_{\varphi}, \qquad \nabla_{2}\Psi = \frac{\partial\Psi}{\partial z}\mathbf{e}_{z} + \frac{\partial\Psi}{\partial r}\mathbf{e}_{r}, \qquad (59)$$

$$\mu_0 J_{\varphi} = -\frac{1}{r} \frac{\partial^2 \Psi}{\partial^2 z} - \frac{\partial}{\partial r} \left(\frac{1}{r} \frac{\partial \Psi}{\partial r} \right). \tag{60}$$

Since the $\nabla_2\Psi$ vector is orthogonal to the surface of constant Ψ , the poloidal magnetic field, $\propto \nabla_2\Psi \times \boldsymbol{e}_{\varphi}$, is parallel to the magnetic surface everywhere, while "j-toroidal-cross-B-poloidal" force,

$$J_{\varphi} \boldsymbol{e}_{\varphi} \times \boldsymbol{B}_{2} = \frac{J_{\varphi}}{r} \nabla_{2} \Psi, \tag{61}$$

is perpendicular to the magnetic surface (i.e., aligned with $\nabla_2\Psi$). This force tends to contract the current filament over the minor radius (i.e., pinch-effect). This contraction may be prevented by the excessive plasma gas-kinetic pressure, P, which tends to expand the filament. To balance the force, described by Equation (61) that is aligned with $\nabla_2\Psi$, the plasma pressure gradient needs to be aligned with $\nabla_2\Psi$ too. The alignment condition, $\nabla_2\Psi\times\nabla_2P=0$ can be identically rewritten in terms of the Jacobian, $D(\Psi,P)/D(z,r)\equiv \frac{\partial\Psi}{\partial z}\frac{\partial P}{\partial r}-\frac{\partial\Psi}{\partial r}\frac{\partial P}{\partial z}$. This Jacobian vanishes identically if, and only if, P is only a function of Ψ , i.e., it is constant at each magnetic surface, so that:

$$-\nabla_2 P = -\frac{dP(\Psi)}{d\Psi} \nabla_2 \Psi. \tag{62}$$

In a low- β plasma, the pinch-effect is mainly prevented by the counteraction of the toroidal magnetic field, B_{φ} , for which the poloidal current density, J_2 , can be expressed in terms of a current function, rB_{φ} :

$$\mu_0 \mathbf{J}_2 = \frac{\nabla_2 (rB_{\varphi})}{r} \times \mathbf{e}_{\varphi}. \tag{63}$$

Again, the current function is required to be constant on magnetic surfaces, and therefore it can be expressed as a function of Ψ only. In this case, the poloidal electric current, $\mathbf{J}_2 = \frac{1}{\mu_0 r} \frac{d(rB_\varphi)}{d\Psi} \nabla_2 \Psi \times \mathbf{e}_\varphi$ is everywhere parallel to the magnetic surface, while the "j-poloidal-cross-B-toroidal" force,

$$\mathbf{J}_{2} \times B_{\varphi} \mathbf{e}_{\varphi} = -\frac{B_{\varphi}}{\mu_{0} r} \frac{d(rB_{\varphi})}{d\Psi} \nabla_{2} \Psi, \tag{64}$$

is perpendicular to the magnetic surface (i.e., aligned with $\nabla_2\Psi$). Summing up, Equations (61), (62), and (64) reduce the LHS of the *vector* equilibrium condition, $J_{\varphi}\boldsymbol{e}_{\varphi}\boldsymbol{B}_{2}+\boldsymbol{J}_{2}\times\boldsymbol{B}_{\varphi}\boldsymbol{e}_{\varphi}-\nabla P=0$, to a linear combination of aligned vectors:

$$\left[\frac{J_{\varphi}}{r} - \frac{(rB_{\varphi})}{\mu_0 r^2} \frac{d(rB_{\varphi})}{d\Psi} - \frac{dP}{d\Psi}\right] \nabla_2 \Psi = 0. \tag{65}$$

For Equation (65) to hold everywhere, the expression in the square bracket must vanish. This condition yields the *scalar* GS equation:

$$\frac{J_{\varphi}}{r} = \frac{(rB_{\varphi})}{\mu_0 r^2} \frac{d(rB_{\varphi})}{d\Psi} + \frac{dP}{d\Psi}.$$
 (66)

The LHS of this equation is often expressed using the RHS of Equation (60), but in the present derivation, this step is not needed.

In equilibrium, the toroidal plasma filament boundary must coincide with a magnetic surface; hence, the total flux function, Ψ , should reach a constant value, $\Psi(u_0)$, at the boundary. Since an arbitrary constant may be added to the total flux function (not to the reduced one!), by not changing the poloidal magnetic field as given by Equation (59), one can claim with no loss in generality that the total flux function must vanish at the filament boundary to satisfy the equilibrium condition and so does the reduced flux function. The latter can only be achieved if the external magnetic field as in Equations (28) and (29) is applied with Fourier harmonics exactly prescribed by the current amplitudes. We arrive at two important points: (1) the filament cannot be in equilibrium by itself; therefore, there must be an external field (this is also a consequence from strict Shafranov's theorem described in Section 5.2); and (2) the exact Grad-Shafranov equilibrium requires a nontrivial distribution of the external field to be exactly prescribed, which for our applications is unrealistic and impractical.

5.2. Shafranov's Virial Theorem and Its Consequences for a Uniform Strapping Field

In Sections 3 and 4 we considered only the magnetic field, B_2 , induced by the current flowing inside the filament. However, when discussing the MHD equilibrium of a circular current filament, one must also consider the Shafranov (1966) virial theorem (see also Faddeev et al. 2002) that states that the magnetic field of the current and the internal plasma pressure of the filament are not sufficient to maintain MHD equilibrium. As pointed out by Landau & Lifshitz (1984), the equilibrium condition, $J \times B - \nabla P = 0$, can be reformulated in terms of the Maxwell stress tensor, Π , with the help of Ampère's law, $\nabla \times B = \mu_0 J$:

$$-\nabla \cdot \mathbf{\Pi} = 0, \quad \mathbf{\Pi} = \left(P + \frac{B^2}{2\mu_0}\right) \mathcal{I} - \frac{\mathbf{B} \otimes \mathbf{B}}{\mu_0}, \quad (67)$$

 \mathcal{I} being the unit tensor. By taking the scalar product of Equation (67) with \mathbf{R} and integrating over the entire volume (the pressure and current density are zero outside the filament, but the magnetic field is not) by parts using the identity, $-\mathbf{R} \cdot (\nabla \cdot \mathbf{\Pi})^T = Tr(\mathbf{\Pi}) - \nabla \cdot (\mathbf{\Pi} \cdot \mathbf{R})$, we obtain that the integral of the LHS of Equation (67) is positive definite:

$$-\int \mathbf{R} \cdot (\nabla \cdot \mathbf{\Pi})^T dV = E > 0,$$

$$E = \int Tr(\mathbf{\Pi}) dV = \int \left(3P + \frac{B^2}{2\mu_0}\right) dV. \tag{68}$$

Since the RHS of Equation (67) is zero, it thus cannot be equal to the LHS, proving that any closed loop configuration is out of equilibrium in the absence of an external magnetic field.

Shafranov's theorem (Equation (68)) in effect states that the *hoop force* results from the interaction between the loop current and its self-generated magnetic field. Even though the integral of this force density $(f^{\text{(hoop)}} = -\nabla \cdot \mathbf{\Pi})$ vanishes over the entire volume $(f^{\text{(hoop)}}) = -\nabla \cdot \mathbf{\Pi} = \mathbf{\Pi}$ vanishes over the entire volume $(f^{\text{(hoop)}}) = -\nabla \cdot \mathbf{\Pi} = \mathbf{\Pi}$ vanishes over the entire volume ($f^{\text{(hoop)}} = -\nabla \cdot \mathbf{\Pi} = \mathbf{\Pi}$), it has a positive average projection to the radial direction $(f^{\text{(hoop)}}) = E > 0$). It is known from experiments (see Yee & Bellan 2000) that the hoop force tends to expand the current loop outward, and in the absence of external fields, this expansion is approximately self-similar. By approximating the velocity of this self-similar expansion as $v = \frac{R}{R_{\infty}} \frac{dR_{\infty}}{dt}$, we see that Equation (68) confirms

the development of an expanding flow, since the growth rate of the kinetic energy, $dE^{(k)}/dt$ is positive:

$$\frac{dE^{(k)}}{dt} = \int v \cdot f^{(hoop)} dV = \frac{E}{R_{\infty}} \frac{dR_{\infty}}{dt} > 0.$$
 (69)

A more traditional derivation of the hoop force can be carried out using the energy principle, assuming that the pressure adiabatically scales with volume as $P \propto V^{-\gamma}$, and considering a particular choice of the polytropic index, $\gamma = 4/3$. Consider a conformal expansion where each point, R, maps to $(\delta R_{\infty}/R_{\infty}+1)R$. In this case, the infinitesimal *virtual displacement* is equal to $\delta R = (\delta R_{\infty}/R_{\infty})R$. For a frozen-in magnetic field, the local magnetic field scales as $\propto (\delta R_{\infty}+R_{\infty})^{-2}$, while the pressure adiabatically scales as $\propto [(\delta R_{\infty}+R_{\infty})^{-2}]$, while the pressure adiabatically scales as $\propto [(\delta R_{\infty}+R_{\infty})^{-2}]$, similarly to the magnetic pressure that scales as $B^2 \propto (\delta R_{\infty}+R_{\infty})^{-4}$ (this is why $\gamma = 4/3$ was chosen). According to general principles, the work done by local forces during the virtual displacement, $\int f^{(\text{hoop})} \cdot \delta R dV$, equals the negative of the variation in the energy integral, $-\delta E = -\delta R_{\infty} \frac{dE}{dR_{\infty}}$:

$$\frac{1}{R_{\infty}} \int \mathbf{R} \cdot \mathbf{f}^{\text{(hoop)}} dV = -\frac{dE}{dR_{\infty}},$$

$$E = \int \left(\frac{P}{\gamma - 1} + \frac{B^2}{2\mu_0}\right) dV = \int \left(3P + \frac{B^2}{2\mu_0}\right) dV, \quad (70)$$

where $\frac{dE}{dR_{\infty}} = -\frac{E}{R_{\infty}}$, because the total energy scales as $\propto (\delta R_{\infty} + R_{\infty})^{-1}$. Even though the energy principle approach does not go beyond the already-derived Equation (68), it allows us to evaluate the energy of the motion driven by the hoop force. Combining Equations (69) and (70), we find that:

$$\frac{dE^{(k)}}{dt} = -\frac{dR_{\infty}}{dt}\frac{dE}{dR_{\infty}} = -\frac{dE}{dt};$$
(71)

hence, $d(E^{(k)} + E)/dt = 0$ and $E^{(k)}(t \to \infty) = E(t = 0)$.

For a thin circular current filament, one can approximate $|\mathbf{R}| \approx R_{\infty}$ in the integrand in Equation (70), providing an estimate for the hoop force per unit toroidal angle:

$$\frac{dF^{\text{(hoop)}}}{d\varphi} \approx \frac{1}{2\pi} \frac{E}{R_{\infty}}.$$
 (72)

Equation (72) follows from Equation (68) and is always valid; however, for $\gamma \neq 4/3$, E on the RHS is not the energy. This approximation connects our approach to the formalism used to describe the hoop force in the literature, (see Equation (5) in Titov & Démoulin (1999) and Equation (2) in Kliem & Török 2006). The main distinction between earlier work and our approach is that our model allows for finite β values (see details in Section 5.5 below).

In application to a CME generator, a current filament can be superposed on top of the model of an active region, so that a "strapping magnetic field" of the active region maintains the equilibrium if it matches the filament geometry and parameters. In the case when the strapping field at the loop location, $B^{(s)}$, is uniform, a slight reformulation of the Shafranov theorem provides an estimate for the strapping field in terms of the filament parameters (or vice versa). Indeed, the integration of the modified equilibrium equation,

 $[-\nabla \cdot \mathbf{\Pi} + \mathbf{J} \times \mathbf{B}^{(s)}] \cdot \mathbf{R} = 0$, gives:

$$E + 2\mathbf{B}_2^{(s)} \cdot \mathcal{M} = 0. \tag{73}$$

where

$$\mathcal{M} = \frac{1}{2} \int \mathbf{R} \times \mathbf{J} dV \tag{74}$$

is the magnetic moment that has already been introduced earlier (see Equation (40)). Equation (73) unambiguously determines the intensity of the uniform strapping field in terms of two integral parameters of the configuration. The direction of the strapping field must be aligned with the magnetic moment; otherwise, a torque, $\mathcal{M} \times \mathbf{B}_2^{(s)} \neq 0$ would act on the loop (see Jackson 1999) breaking the equilibrium. For axisymmetric current configurations, the magnetic moment is parallel to the axis of symmetry,

$$\mathcal{M} = \mathcal{M} \mathbf{e}_z, \qquad \mathcal{M} = \frac{1}{2} \int r J_{\varphi} dV.$$
 (75)

It follows that the strapping field, $B^{(s)}e_z$, must also be parallel to the axis of symmetry. For an axisymmetric configuration, the square of the magnetic field can be decomposed to contributions from poloidal and toroidal fields, $B^2 = B_{\varphi}^2 + [\nabla \times (A_{\varphi}e_{\varphi}]^2$, and thus reduce Equation (73) to the following form:

$$\int \left(\frac{J_{\varphi}A_{\varphi}}{2} + \frac{B_{\varphi}^{2}}{2\mu_{0}} + 3P \right) dV + 2B^{(8)}\mathcal{M} = 0, \tag{76}$$

where the integrand is nonzero only inside the filament, simplifying the integration.

Identifying a circular arc inside an active region at which the magnetic field is uniform and orthogonal to the plane of the arc, choosing the loop parameters depending on thus determined strapping field and inserting this current loop along this arc is at the heart of the Titov et al. (2014) CME generator. Our approach allows us to generalize the Titov et al. (2014) model and to extend it to finite β current loops. This will be achieved by considering a detailed derivation of Equation (73) from the local equilibrium condition specified for a particular class of n=0 harmonic field as discussed below in Sections 5.3 and 5.4.

5.3. Reduced Grad–Shafranov Equation in Toroidal Coordinates

In general, to find the conditions under which a plasma in the magnetic field of the n=0 harmonic is in force equilibrium, one needs to solve the Grad–Sharfranov equation in toroidal coordinates. Some of these solutions are known (see, e.g., Zakharov & Shafranov 1986); however, they include infinite series of harmonics and require highly complicated strapping fields. While in application to laboratory plasmas, such specially designed confining magnetic fields are not unusual, nature does not implement such special analytic solutions.

Here, we use a simpler approach and reduce the GS equation in toroidal coordinates by assuming that, rather than finding magnetic surfaces where the true flux function, Ψ , is constant, their role in the formalism can be partly substituted by considering "constant ψ -surfaces," where the reduced flux function, $\psi(u, v)$, is constant. In the particular case of the n = 0

harmonic field, $\psi(u, v)$ is a function of u only; hence, these surfaces are toroidal coordinate surfaces of constant u.

Note that constant ψ -surfaces are not magnetic surfaces, since the true flux function, $\Psi = \mu_0 \sqrt{R_\infty r} \psi$, (see Equation (3)) is not constant at constant ψ , and $\nabla_2 \Psi$ is not orthogonal to constant ψ -surfaces, because of the explicit dependence of Ψ on r. In addition to the magnetic field generated by the filament current and characterized by ψ function, the effect of the strapping field, $\mathbf{B}_2^{(s)} = \mathbf{B}^{(s)} \mathbf{e}_z$, should be explicitly added to the net force balance, $\mathbf{J}_2 \times (\mathbf{B}_2 + \mathbf{B}^{(s)} \mathbf{e}_z) - \nabla P = 0$. Now, we can use Equation (12) for the magnetic field and Equation (4) for the toroidal current density to describe the pinch-effect force in Equation (61):

$$J_{\varphi} \boldsymbol{e}_{\varphi} \times (\boldsymbol{B} + B^{(s)} \boldsymbol{e}_{z}) = \frac{j(u, v) R_{\infty}}{r^{4}} \times \left[\mu_{0} r \nabla_{2} \psi + \left(\frac{\mu_{0} \psi}{2} + \frac{r^{\frac{3}{2}}}{R_{\infty}^{\frac{1}{2}}} B^{(s)} \right) \boldsymbol{e}_{r} \right].$$
(77)

The dominant contribution to the force in Equation (77) is directed along $\nabla_2 \psi$, hence, orthogonal to the constant ψ -surface. Following the basic idea of the GS equation, we parameterize the toroidal field, B_{φ} , and gas-kinetic pressure, P, in terms of the representative functions of ψ , $B_{\varphi}^2 = b^2(\psi)(R_{\infty}/r)^3$ and $P = p(\psi)(R_{\infty}/r)^3$. The total force produced by B_{φ} and P is given by the sum of Equations (62) and (64):

$$\frac{\left[\nabla_{2}(rB_{\varphi}) \times \boldsymbol{e}_{\varphi}\right] \times B_{\varphi}\boldsymbol{e}_{\varphi}}{\mu_{0}r} - \nabla_{2}P = \frac{R_{\infty}^{3}}{r^{4}}$$

$$\times \left[-r\frac{dp^{\text{tot}}}{d\psi}\nabla_{2}\psi + (p^{\text{tot}}(\psi) + 2p(\psi))\boldsymbol{e}_{r}\right].$$
(78)

We note that the gradient of the total pressure, $p^{\rm tot} = p + b^2/(2\mu_0)$ is orthogonal to constant ψ -surfaces in Equation (78). Similarly to Equation (65), the total force, given by the sum of Equations (77) and (78) vanishes in equilibrium if the following equation holds:

$$\frac{R_{\infty}}{r^4} \left(\mu_0 j - R_{\infty}^2 \frac{dp^{\text{tot}}}{d\psi} \right) r \nabla_2 \psi
+ \left[\frac{J_{\varphi} A_{\varphi}}{2} + \frac{B_{\varphi}^2}{2\mu_0} + 3P + r J_{\varphi} B^{(8)} \right] \frac{\mathbf{e}_r}{r} = 0.$$
(79)

In Equation (79) the dominant force comes from the pincheffect and its opposing pressure gradient. This term is proportional to $\nabla_2 \psi$ (i.e., it is normal to $\psi = \text{const surfaces}$). This dominant force vanishes identically if the *reduced* version of the GS equation (Equation (66)) holds:

$$j = \frac{R_{\infty}^2}{\mu_0} \frac{dp^{\text{tot}}}{d\psi}.$$
 (80)

The reduced GS equation ensures equilibrium against the pinch-effect, similarly to the full equation (see Equation (66)). However, because of the combined effect of the strapping field and of the r-dependent factors in the definitions of the ψ -function and the representative functions, $p(\psi)$, $b(\psi)$, there is also a force directed along e_r in Equation (79). The whole point of the proposed approach is that while balancing the pinch-

effect from the analytically known current and magnetic field can be exactly solved with the help of the reduced GS equation as demonstrated in the present subsection, the condition for the radially directed force in Equation (79) to vanish,

$$\left[\frac{J_{\varphi}A_{\varphi}}{2} + \frac{B_{\varphi}^{2}}{2\mu_{0}} + 3P + rJ_{\varphi}B^{(s)} \right] \frac{e_{r}}{r} = 0, \tag{81}$$

cannot be satisfied *locally* with any physically admissible (divergence-free and curl-free) strapping field, including the uniform strapping field considered here. In CME generation, the situation is even more complicated, because the *local* values of realistic strapping fields are not known. However, a *global* balance for an integral radial force (which is in effect the integrand of Equation (76)) can be achieved if the strapping field satisfies Equation (76), as we will discuss in Section 5.4 below

Next, we consider the solution of the reduced GS equation for the current distribution described in Section 4 that depends only on u, $j(u, v) = j_0(u)$. Equation (80) can be expressed in terms of the normalized quantities, $\tilde{\psi}(u)$, $\tilde{j}(u)$, and the characteristic field, B_c , (see Equations (22) and (32)) and then integrated over u:

$$p^{\text{tot}}(u) = 8 \frac{B_c^2}{2\mu_0} \int_{u_0}^{u} \tilde{j}(u_1) \frac{d\tilde{\psi}}{du_1} du_1.$$
 (82)

Here, we note that in the absence of an external toroidal field and pressure, the quantity, $p^{\text{tot}}(u_0)$, vanishes. An *important* feature of our approach is that the plasma parameter β ,

$$\beta = \frac{p(u)}{b^2(u)/(2\mu_0)} = \text{const}, \tag{83}$$

is assumed to be constant, but finite, so that the toroidal field and gas-kinetic pressure can be expressed in terms of the total pressure:

$$\frac{b^2}{2\mu_0} = \frac{p^{\text{tot}}(u)}{1+\beta}, \quad p(u) = \frac{\beta p^{\text{tot}}(u)}{1+\beta}.$$
(84)

Using Equation (82), this can be expressed in terms of the dimensionless toroidal field amplitude, $B^{(tor)}$:

$$p^{\text{tot}}(u) = \frac{[B^{(\text{tor})}(u)B_c]^2}{2\mu_0},$$

$$B^{(\text{tor})}(u) = \sqrt{8 \int_{u_0}^{u} \tilde{j}(u_1) \frac{d\tilde{\psi}}{du_1} du_1}.$$
(85)

For the current and reduced flux functions given by Equations (46) and (54), the integral in Equation (85) can be carried out by parts using Equation (A18):

$$[B^{(\text{tor})}(u)]^{2} = 8\tilde{j} (u_{1}) [\tilde{\psi}(u_{1}) - \tilde{j}_{E}(u_{1})]|_{u_{0}}^{u} + \frac{8}{E^{(0)}} \frac{d\tilde{\psi}(u)}{d \coth u} \frac{d}{du_{1}} [\tilde{\psi}(u_{1}) - \tilde{j}_{E}(u_{1})]|_{u_{0}}^{u} + \frac{4\tilde{j}^{2}(u_{1})}{E^{(1)}}|_{u_{0}}^{u}.$$

$$(86)$$

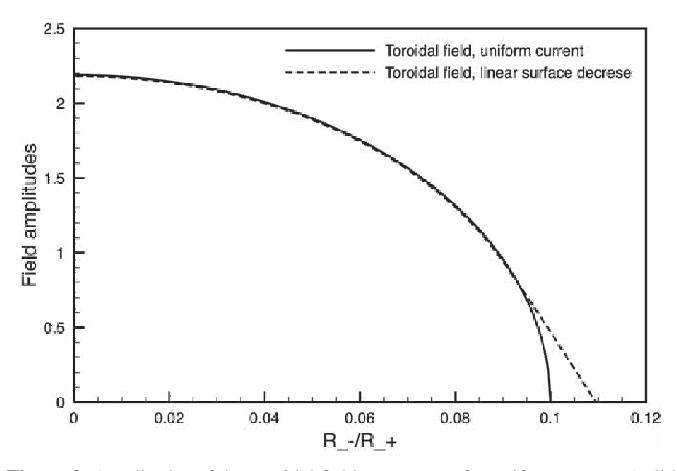


Figure 3. Amplitudes of the toroidal field component for uniform current (solid line) and for linear surface decrease current (dashed line), for the same filament and in the same coordinate as used in Figure 2.

For a uniform current form factor, as in Equation (51), using Equations (44) and (54), one obtains the following:

$$B^{(\text{tor})}(u > u_0) = \sqrt{\ell^{(\text{tor})}(u_0)[\bar{Q}_{-\frac{1}{2}}^{-1}(u_0) - \bar{Q}_{-\frac{1}{2}}^{-1}(u)]},$$

$$\ell^{(\text{tor})}(u_0) = 8 \left[\frac{\tilde{j}_E(u_0)}{\bar{Q}_{-\frac{1}{2}}^{-1}(u_0)} - \ell^{(s)}(u_0) \right] \tilde{j}(u_0), \tag{87}$$

where $\ell^{\text{(tor)}}$ is another induction coefficient, which is discussed below (see Section 5.5) to characterize the energy of toroidal magnetic field, expressed in terms of the current density $\tilde{j}(u_0) = \frac{3}{4}\tilde{j}_E(u_0)$ and $\tilde{j}_E(u_0)$ given by Equation (55). The toroidal field amplitude for the uniform current form factor given by Equation (87) is shown in Figure 3 with the solid line. For the current form factor with linear surface decrease given by Equation (53), the toroidal field near the filament boundary can be calculated by applying the general formula in Equation (86) to the reduced flux function given by Equation (56). Thus, calculated toroidal field amplitude is shown in Figure 3 with the dashed line. A comparison of the curves in Figure 3 shows how the singularity in the toroidal field near the boundary (infinite spatial derivative of the solid line as $\kappa' \to \kappa'_0$) is eliminated by using a linearly decreasing current near the surface (dashed line).

Equation (85) allows us to express the total magnetic field (including the toroidal component) that satisfies the reduced GS equation:

$$\mathbf{B}_{0} = \frac{R_{\infty}^{\frac{3}{2}}}{r^{\frac{3}{2}}} B_{c}
\times \left[B^{(z)}(u) \mathbf{e}_{z} \pm \frac{B^{(tor)}(u)}{\sqrt{1+\beta}} \mathbf{e}_{\varphi} - \left[\frac{B^{(p)}(u)}{\kappa'} \right] (\kappa' \mathbf{e}_{v}) \right], \quad (88)$$

where $\mathbf{e}_{\varphi} = \mathbf{e}_z \times \mathbf{R}/r$. Since the toroidal field amplitude, $B^{(\text{tor})}(u)$, is positive as is the toroidal current density, $j_0(u)$, the choice of plus or minus sign in Equation (88) corresponds to the positive or negative *helicity*, $\operatorname{sign}(B_{\varphi}/J_{\varphi})$. The magnetic field calculated using Equation (39) for $\kappa \leqslant \kappa_0$ and with Equation (88) for $\kappa \geqslant \kappa_0$ and with field amplitudes obtained

assuming uniform current form factor is shown in Figure 4 for $R_{\infty}=1, \, \kappa_0'=0.1.$

This magnetic field produced by an azimuthal current (white magnetic field lines) and magnetic field inside the toroidal filament (red and blue color) satisfies the reduced GS equation. However, the right (zoomed) panel demonstrates that the equilibrium is not yet complete. As emphasized in Section 5.1, under equilibrium conditions, the (yellow) boundary of the filament, where the total pressure turns to zero (hence it is constant), must coincide with a magnetic surface. Inspection of Figure 4 shows that magnetic surfaces defined by closed (poloidal) magnetic field lines (white lines) intersect the plasma boundary (yellow circle) at multiple locations, indicating the absence of true equilibrium.

For constant β , one can find the corresponding gas-kinetic pressure inside the filament using Equation (85):

$$P(u \geqslant u_0) = \frac{\beta}{1+\beta} \frac{R_{\infty}^3}{r^3} \frac{[B^{(\text{tor})}(u)B_c]^2}{2\mu_0}.$$
 (89)

Assuming constant electron and ion temperatures inside the filament, T_e and T_i , one can also derive the distribution of plasma density that will form the ejecta:

$$\rho(u \geqslant u_0) = \frac{\beta}{1+\beta} \frac{R_{\infty}^3}{r^3} \frac{[B^{(\text{tor})}(u)B_c]^2 m_i}{2\mu_0 k_{B(T_i + Z_i T_e)}},\tag{90}$$

where m_i and Z_i are the average mass and charge state of ions, and k_B is the Boltzmann constant. An equation for the Alfvénwave speed in the φ -direction,

$$V_{A,\varphi}^2 = \frac{B_{\varphi}^2}{\mu_0 \rho} = \frac{2k_{B(T_i + Z_i T_e)}}{\beta m_i},$$
(91)

directly follows from Equation (90). This useful parameter is constant as long as β , T_i , and T_e are assumed to be constant.

The total ejected mass can be expressed in terms of the total pressure integral over the filament volume:

$$M = \int \rho dV = \frac{2\int \left(P + \frac{B_{\varphi}^2}{2\mu_0}\right) dV}{(1+\beta)V_{A,\varphi}^2},\tag{92}$$

which is calculated and discussed in Section 5.5.

5.4. Balancing the Hoop Force by a Strapping Field

We demonstrated that the reduced GS equation (Equation (80)) ensures the cancellation of the dominant pinching force at *each point* inside the filament. However, in the full force balance, there is an unbalanced radial force described by Equation (81) that does not vanish *locally*. The first three terms in Equation (81) describe the density of the *hoop force* directed radially outward (compare them with the integrand in Equation (76)). This force is fully determined by the parameters of the plasma configuration. The last term in Equation (81) describes the effect of the strapping field on the toroidal current, which may oppose the hoop force if the strapping field is negative (i.e., antiparallel to the magnetic moment).

Since the hoop force density and the current density are different functions of the coordinates, the local forces cannot be balanced by a uniform strapping field. Alternatively, if we express the strapping magnetic field from Equation (81), both

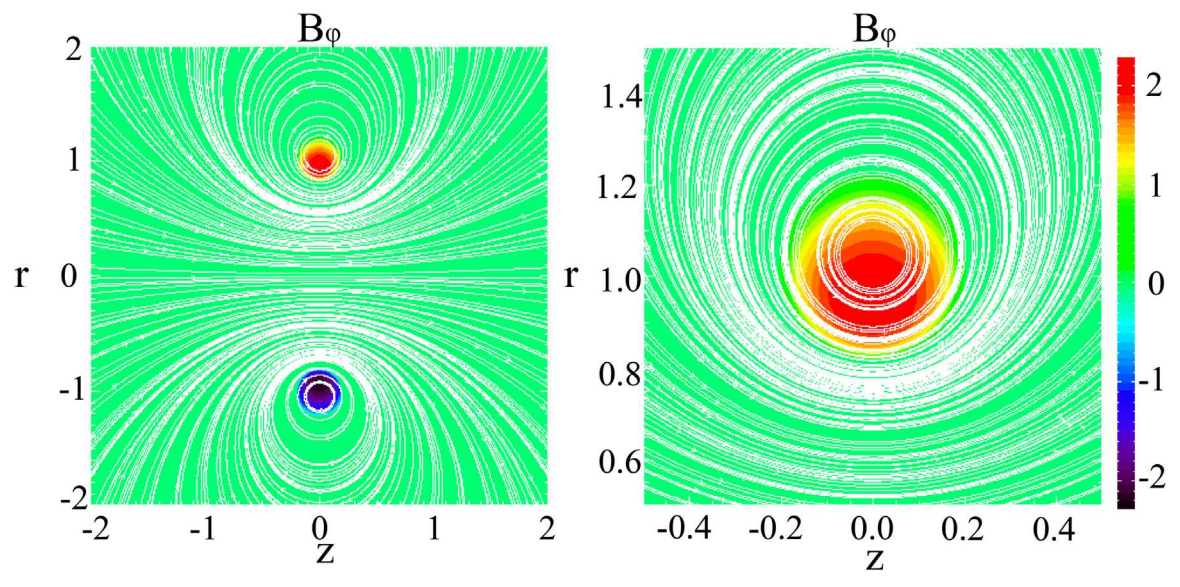


Figure 4. Left panel: solution of the reduced GS equation, in the meridional cross section (z, r plane), for $R_{\infty} = 1$, $\kappa'_0 = 0.1$, $B_c = 1$ and positive helicity. White lines: field lines of the poloidal field (B_z, B_r) . Color: toroidal magnetic field, B_{φ} , perpendicular to the image plane, outgoing field being positive, incoming one being negative. The figure corresponds to positive helicity; otherwise, the blue and red circles would swap. Right panel: close-up image of the cross section of the plasma filament.

the divergence and the curl of this field would not vanish. This situation can be rectified by ensuring that *global equilibrium*, holds, i.e., requiring that the integrated radial force (given by Equation (81)) vanishes over the plasma volume. This means that the integrated hoop force is balanced by the overall effect of the adjusted strapping field. This can be achieved by taking the scalar product of Equation (81) and R and integrating the resulting scalar equation over the entire plasma volume. This way, we obtain Equation (76) as an integral radial force balance equation, unambiguously determining the strapping field:

$$\int \left(\frac{J_{\varphi} A_{\varphi}}{2} + \frac{B_{\varphi}^2}{2\mu_0} + 3P \right) dV + 2\pi R_{\infty}^2 I^{\text{tot}} B^{(s)} = 0, \quad (93)$$

where in Equation (76) we substituted Equation (40) for the magnetic moment, \mathcal{M} . As we discussed in Section 5.2, in the absence of a strapping field, $B^{(s)}=0$, the radial hoop force (parameterized by the volume integral of a function that is positive definite everywhere) would disrupt the current filament over the major radius. However, the Ampère force from the strapping field, $(J_{\varphi} e_{\varphi}) \times (B^{(s)} e_z) = J_{\varphi} B^{(s)} e_r$, tends to contract the filament in case $B^{(s)} < 0$, and it may balance the hoop force. The condition for the force balance can be parameterized in terms of the inductance, L_0 , since the volume integral evaluating the hoop force in Equation (93) is very close to the magnetic free energy (exactly coincides with that for $\gamma = 4/3$ —see Section 5.2 for more details):

$$B^{(s)} = -\frac{L_0 I^{\text{tot}}}{4\pi R_{\infty}^2} = -\frac{1}{2\pi} \frac{L_0}{\mu_0 R_{\infty}} B_c,$$

$$\frac{L_0 (I^{\text{tot}})^2}{2} = E_0 = \int \left(\frac{J_{\varphi} A_{\varphi}}{2} + \frac{B_{\varphi}^2}{2\mu_0} + 3P \right) dV. \tag{94}$$

The strapping field is antiparallel to the B_c field, and its magnitude can be derived from the inductance. Equation (94) shows that in order to derive the strapping field that is needed

for obtaining full equilibrium solutions, one has calculate the inductance for the given current density profile. This derivation is discussed in Section 5.5.

In Figure 5 we consider the same configuration as in Figure 4 $(R_{\infty} = 1, \kappa'_0 = 0.1)$, but with a superposed uniform strapping field given by Equation (94) (the inductance for n = 0 is determined by Equation (108), discussed below). The left panel shows a drastically changed topology compared to the nostrapping-field configuration in Figure 4. The separator surface separates the external region of the strapping field from the region of the field generated by the filament current. In the right panel, the coincidence of the filament boundary (yellow color) with a magnetic surface (white line) demonstrates that in the presence of a strapping field, this equilibrium condition is satisfied, while in the configuration with no-strapping field (see Figure 4), this condition is not met.

Alternatively, the equilibrium condition can be verified if the near-equilibrium magnetic field (given by Equation (88)), gaskinetic pressure (Equation (89)), and density (Equation (90)) distributions are used as the initial condition for the Relaxation MagnetoHydroDynamics (R-MHD) model. In this model, an artificial friction force density, $-\rho U/\tau$, is added to the momentum equation, which is oppositely directed than the plasma velocity vector, U. The friction force relaxes the residual plasma motions with a characteristic time of $\tau=$ const, thus damping the possible oscillations around the equilibrium state.

The result of such a simulation is presented in Figure 6. The initial condition corresponds to a current filament with major and minor radii of $R_0 = 0.202/0.99R_{\odot}$, $a = 0.04/0.99R_{\odot}$, so that $R_{\infty} = 0.1R_{\odot}$ and $\kappa'_0 = 0.1$. The horizontal (z) and vertical (r) coordinates are also measured in units of solar radii, R_{\odot} . The uniform strapping field is chosen to be $B^{(s)} = 2.7$ G, while the current is $I^{\text{tot}} \approx 1.5 \times 10^{11}$ A, expressed in terms of the strapping field using the equilibrium condition, Equation (94). The other parameters are $T_e = T_i = 5 \times 10^5$ K and $\beta = 0.1$. As we recommend for any application, the uniform current form factor is used with linear surface decrease in a narrow region

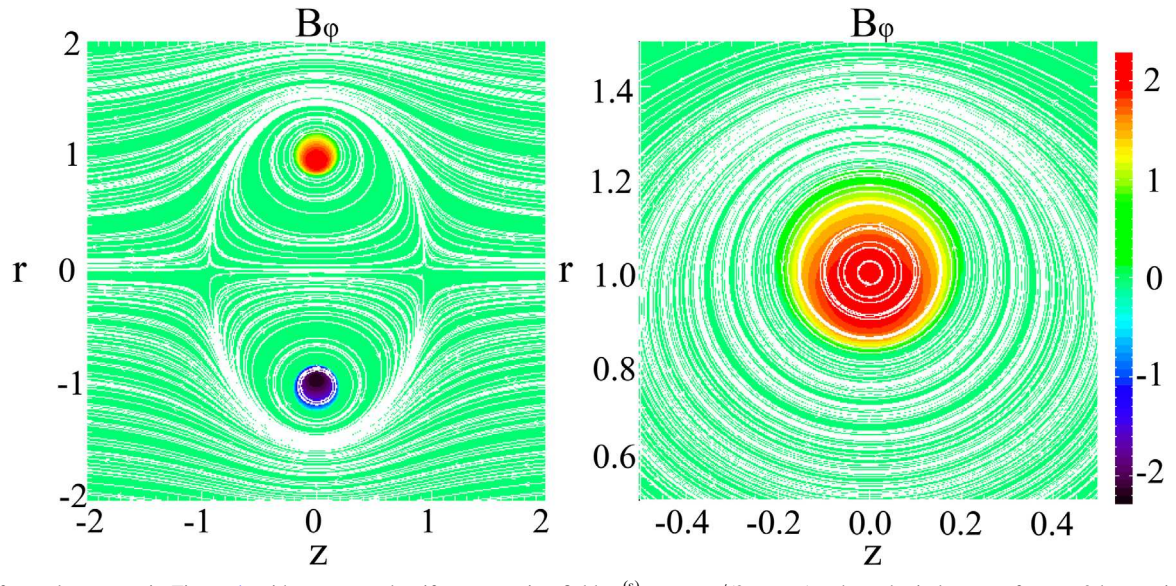


Figure 5. Left panel: same as in Figure 4, with superposed uniform strapping field, $B^{(s)} = -L_0B_c/(2\pi\mu_0R_\infty)$, where the inductance for n=0 harmonics is given by Equation (108) below. White lines: field lines of the poloidal field (B_z, B_r) . Color: toroidal magnetic field, B_φ , perpendicular to the image plane, the outgoing field being positive, and the incoming one being negative. The figure corresponds to positive helicity; otherwise, the blue and red circles would swap. Right panel: close-up image of the cross section of the plasma filament. Coincidence of the filament boundary (yellow color) with the magnetic surface (white line) demonstrates that the equilibrium condition is satisfied.

 $(\varepsilon=0.1)$; however, the inductance characterizing equilibrium strapping field is calculated for purely uniform current $(\varepsilon=0)$.

The meridional cross section of the initial field distribution is shown in the left panel of Figure 6. The white circles show the closed magnetic field lines of the poloidal field (=the meridional cross sections of the magnetic surfaces), with the color scale showing the levels of $rB_{\varphi}\left[G\cdot R_{\odot}\right]$ (=constant levels of the poloidal current function). While the exact Grad–Shafranov equation requires the poloidal current function to be constant at magnetic surfaces (see Section 5.1 for more detail), in the initial plasma configuration there is a slightly visible misalignment between the level contours of the current function and the magnetic surfaces.

Using this initial condition, we integrate the axisymmetric R-MHD equations with a relaxation time of $\tau = 1 \times 10^3$ s, on a grid of 1000 × 500 cells covering the coordinate range of $-0.5R_{\odot} \leqslant z \leqslant 0.5R_{\odot}$, $0 \leqslant r \leqslant 0.5R_{\odot}$, to evolve the initial distribution for $t = 6 \times 10^3$ s. A background plasma of negligible pressure but finite density is added outside the filament to limit the characteristic speeds of the MHD perturbations and avoid too small time steps. The result of the numerical simulation is presented in the right panel of Figure 6. Perfect alignment of the current function levels with the magnetic surfaces demonstrates that the plasma filament reached equilibrium. The video file shows that the relaxation to equilibrium proceeds via damping of small-amplitude internal oscillations, with no collapse by the pinch-effect (prevented by the counter-pressure of the toroidal field) and no disruption by the hoop force (prevented by the strapping field).

5.5. Magnetic Energy and Inductance

A contribution to the integral in Equation (94) determining the strapping field from the free energy of the poloidal magnetic field, $E^{(p)} = \frac{1}{2} \int J_{\varphi} A_{\varphi}(2\pi r) H_{\nu} H_{u} d\nu du$, can be

derived from Equations (5), (14), and (15):

$$E^{(p)} = \pi R_{\infty} \mu_{0} \int \frac{j(u, v) \psi(u, v)}{\sinh^{2} u} du dv$$

$$= 2\pi^{2} R_{\infty} \mu_{0} \sum_{n=-\infty}^{\infty} \int_{u_{0}}^{\infty} \frac{i_{n}^{*}(u) \psi_{n}(u)}{\sinh^{2} u} du$$

$$= \frac{1}{2} \sum_{n=-\infty}^{\infty} (L_{n}^{(\text{ext})} + L_{n}^{(\text{int})}) |I_{n_{0}}|^{2},$$
(95)

where the external field inductance,

$$\frac{L_n^{\text{(ext)}}}{\mu_0 R_\infty} = \frac{4\pi^2 \tilde{\psi}(u_0)}{\bar{Q}_{n-\frac{1}{2}}^{-1}(u_0)} = 4\pi^2 \frac{\left(\frac{1}{8} - \frac{n^2}{2}\right) \bar{P}_{n-\frac{1}{2}}^{-1}(u_0)}{\bar{Q}_{n-\frac{1}{2}}^{-1}(u_0)},\tag{96}$$

(see Equation (26)) quantifies the energy of the magnetic field produced by surface currents concentrated on the filament boundary. In the particular case of n=0 harmonic, the external inductance,

$$\frac{L_0^{\text{(ext)}}}{\mu_0 R_\infty} = 4\pi^2 \ell^{(s)}(u_0) = \frac{\pi^2}{2} \frac{\frac{\bar{P}_{-1}^{-1}(u_0)}{-\frac{1}{2}}}{\bar{Q}_{-\frac{1}{2}}^{-1}(u_0)},\tag{97}$$

(see Equations (44) and (96)) is shown in Figure 7 (solid black curve). For a thin filament ($\kappa'_0 \to 0$), the toroidal functions in Equation (97) can be approximated with the help of Equations (A6) and (A7):

$$\frac{L_0^{\text{(ext)}}}{\mu_0 R_\infty} \approx \log\left(\frac{4}{\kappa_0'}\right) - 2,$$

$$\frac{L_{\pm 1}^{\text{(ext)}}}{\mu_0 R_\infty} \approx \frac{2}{(\kappa_0')^2},$$
(98)

(see the dashed black curve in Figure 7). Comparison of the green and magenta curves in Figure 7 shows that the accuracy

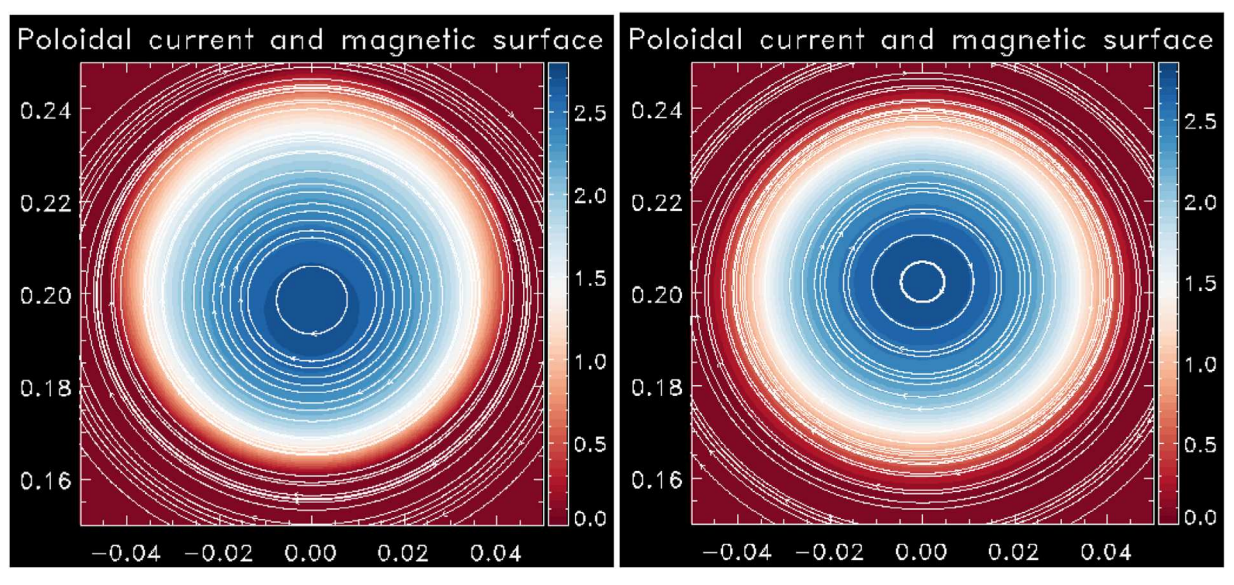


Figure 6. Close-up image of the meridional cross section of the plasma filament. The z, r coordinates are measured in units of R_{\odot} . White curves: closed field lines of the poloidal field (B_z, B_r) (=meridional cross sections of the magnetic surfaces). Color: level contours of the poloidal current function, rB_{φ} , in $G \times R_{\odot}$. Left panel: initial, close to equilibrium field distribution given by Equation (88). Slight misalignment between the levels of the current function and magnetic surfaces demonstrate imperfection of estimated equilibrium. Right panel: same quantities are visualized after relaxation to "true" equilibrium after 6000 s simulation with the R-MHD equations. Perfect alignment of the constant current surfaces with magnetic surfaces demonstrate that the configuration reached the equilibrium state, which is reasonably close to the estimated one. An animation of this figure is available. The animation starts at 0 s and end 6000 s later. The real-time duration of the animation is 6 s.

(An animation of this figure is available.)

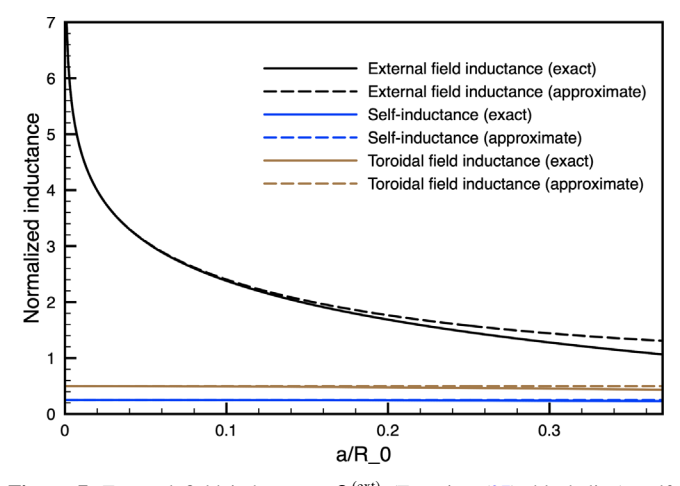


Figure 7. External field inductance, $L_0^{(\text{ext})}$ (Equation (97), black line), self-inductance, $L_0^{(\text{int})}$ (Equation (101), blue line), and toroidal field inductance, $L_0^{(\text{tor})}$ (Equation (106), brown line), for the n=0 harmonic. The normalized inductance coefficients are related to $\mu_0 R_\infty$ and are presented as functions of the $a/R_0 = 2\kappa_0'/(1 + \kappa_0)$ ratio. The functions and their arguments are all

calculated in terms of the value of κ'_0 at the toroidal surface. For comparison, approximate solutions given by Equations (98), (102), and (107) are shown by the dashed lines.

of this approximation for a thin filaments is good enough to make it attractive for CME modeling.

Another contribution to the poloidal field energy is characterized by the positive definite self-induction coefficient, which we calculate only for the n=0 harmonic:

$$\frac{L_0^{(\text{int})}}{\mu_0 R_{\infty}} = 4\pi^2 \int_{u_0}^{\infty} \frac{\tilde{j}(u)\tilde{\psi}(u)}{\sinh^2 u} du - \frac{L_0^{(\text{ext})}}{\mu_0 R_{\infty}}.$$
 (99)

For the manufactured current profile given by Equation (46) and the reduced flux function from Equation (54), the

integration in Equation (99) can be done using Equation (A18):

$$\frac{L_0^{\text{(int)}}}{\mu_0 R_\infty} = 4\pi^2 \left[\int_{u_0}^\infty \frac{\tilde{j}(u)\tilde{j}_E(u)du}{\sinh^2 u} - \frac{\tilde{j}_E(u_0)}{\bar{Q}_{-\frac{1}{2}}^{-1}(u_0)} \right]. \tag{100}$$

In the case of a uniform form factor (see Equation (55)), the limiting value of the self-inductance coefficient for thin filaments (i.e., $u_0 \rightarrow \infty$ and $\kappa'_0 \rightarrow 0$) can be obtained if we de-normalize the currents the following way:

$$\frac{L_0^{(\text{int})}}{\mu_0 R_\infty} = \frac{4\pi^2}{\bar{Q}_{-\frac{1}{2}}^{-1}(u_0)} \times \frac{\tilde{j}(u_0)\tilde{j}_E(u_0)\bar{Q}_{-\frac{1}{2}}^{-1}(u_0)(\coth u_0 - 1) - \tilde{j}_E(u_0)I(u_0)}{I^2(u_0)}, \quad (101)$$

and then apply L'Hôpital's rule to the second fraction. By differentiating both numerator and denominator over du_0 at constant \tilde{j} and \tilde{j}_E , and by using Equation (19) to derive $dI(u_0)/du_0$ and Equation (47) to express $d\bar{Q}_{-\frac{1}{2}}^{-1}(u_0)/du_0 = -I(u_0)/j_E(u_0)$, one finds:

$$u_0 \lim_{M \to \infty} \frac{L_0^{\text{(int)}}}{\mu_0 R_\infty} = \lim_{M \to \infty} \frac{4\pi^2}{\bar{Q}_{-\frac{1}{2}}^{-1}(u_0)} \times \frac{1}{2(\coth u_0 + 1)\bar{Q}_{-\frac{1}{2}}^{-1}(u_0)} = \frac{1}{4},$$
 (102)

since according to Equation (A7) $\bar{Q}_{-\frac{1}{2}}^{-1}(u_0 \to \infty) = 2\pi$.

The rest of the integral, E_0 , determining the strapping field in Equation (94) for constant plasma β , can be expressed in terms

of the integral of total pressure:

$$E_{0} = \frac{1}{2} \left(L_{0}^{\text{(ext)}} + L_{0}^{\text{(int)}} + \frac{1+3\beta}{1+\beta} L_{0}^{\text{(tor)}} \right) (I^{\text{tot}})^{2},$$

$$\int \left[\frac{B_{\varphi}^{2}}{2\mu_{0}} + P \right] dV = \frac{1}{2} L_{0}^{\text{(tor)}} (I^{\text{tot}})^{2}.$$
(103)

The integrand in Equation (103), describing the magnetic free energy density due to the toroidal field, can be calculated by multiplying the representative function, $p^{\text{tot}}(u)$ for the total pressure (see Equation (85)) by $(R_{\infty}/r)^3$ while the volume element equals $dV = H_u H_v 2\pi r du \, dv$. Integrating over $du \, dv$ using Equations (32) and (85) results in the following:

$$\frac{L_0^{\text{(tor)}}}{\mu_0 R_{\infty}} = \pi^2 \int_{u_0}^{\infty} \frac{[B^{\text{(tor)}}(u)]^2}{\sinh^2 u} du.$$
 (104)

In the special case of a uniform current form factor, this expression can be rewritten using Equation (87):

$$\frac{L_0^{\text{(tor)}}}{\mu_0 R_\infty} = \pi^2 \ell^{\text{(tor)}}(u_0) \int_{u_0}^\infty \frac{\bar{Q}_{-\frac{1}{2}}^{-1}(u_0) - \bar{Q}_{-\frac{1}{2}}^{-1}(u)}{\sinh^2 u} du, \quad (105)$$

or, by simplifying Equation (87) using Equations (44), (55), and (A12):

$$\frac{L_0^{\text{(tor)}}}{\mu_0 R_\infty} = \pi^2 \frac{d\bar{P}_{-\frac{1}{2}}^{-1}(u_0)}{du_0} \times \frac{\tilde{J}(u_0)\tilde{J}_E(u_0)\tilde{Q}_{-\frac{1}{2}}^{-1}(u_0)(\coth u_0 - 1) - \tilde{J}_E(u_0)I(u_0)}{I^2(u_0)}.$$
(106)

In the approximation of thin filament, we have

$$u_0 \lim_{\to \infty} \frac{d\bar{P}_{-\frac{1}{2}}^{-1}(u_0)}{du_0} = \frac{4}{\pi}, \quad u_0 \lim_{\to \infty} \frac{L_0^{\text{(tor)}}}{\mu_0 R_\infty} = \frac{1}{2}, \quad (107)$$

according to Equations (A5) and (A6) and analogous derivations for Equation (101) above. Comparison of the exact (solid lines) and approximate (dashed lines) expressions for the self-inductance and toroidal field inductance in Figure 7 shows that the differences between the exact solutions and the approximate ones are hardly visible; therefore, it is fully adequate to use the approximate solutions. With these simplifications, the inductance of the n = 0 harmonic field, determining the magnitude of hoop force, strapping field, and, for a specific adiabatic index, also a magnetic free energy can be obtained with the help of Equations (97) (102), (103), and (107):

$$E_0 = \frac{1}{2} L_0 (I^{\text{tot}})^2,$$

$$L_0 = L_0^{(\text{ext})} + c_{\frac{3}{2}} \mu_0 R_{\infty},$$
(108)

where

$$c_{\frac{3}{4}} = \frac{3}{4} + \frac{\beta}{1+\beta},\tag{109}$$

is a frequently used constant, turning to 3/4 as $\beta \rightarrow 0$. The expression for the hoop force, Equation (72) with the energy integral given by Equation (108) can be compared with that

found in literature (see Equation (5) in Titov & Démoulin (1999) and Equation (2) in Kliem & Török 2006). The (inessential) difference of our approach is in the use of the exact Equation (44) for the external field inductance instead of the approximate Equation (98) and in the term allowing for, if desired, the contribution from the gas-kinetic pressure. However, the difference is small, which justifies our model.

5.6. Improved Equilibrium Theory for a Thin Filament

For a thin filament, the equilibrium condition can be simplified, allowing us to improve the accuracy of the solution and get it much closer to a real equilibrium. To achieve this, we reevaluate the condition under which the sum of Equations (77) and (78) vanishes,

$$\sinh u \left[\left(\tilde{j} \frac{d\tilde{\psi}}{du} - \frac{\partial \tilde{p}^{\text{tot}}}{\partial u} \right) \mathbf{e}_{u} - \frac{\partial \tilde{p}^{\text{tot}}}{\partial v} \mathbf{e}_{v} \right] + \left(\frac{\tilde{j} \tilde{\psi} - \tilde{p}^{\text{tot}}}{2} + \frac{r^{\frac{3}{2} \frac{3}{2} \infty}}{R} \frac{\tilde{j} B^{(s)}}{2B_{c}} + \frac{3\tilde{b}^{2}}{4} + \frac{7\tilde{p}}{2} \right) \mathbf{e}_{r} = 0, \tag{110}$$

where: (1) similar to the dimensionless representative functions for current and flux, \tilde{j} , $\tilde{\psi}$, we introduced analogous functions for the pressures and magnetic field:

$$\tilde{p}^{\text{tot}} = \frac{\tilde{b}^2}{2} + \tilde{p}, \quad \tilde{p} = \frac{R_{\infty}^2 p}{\mu_0 (I^{\text{tot}})^2}, \quad \tilde{b} = \frac{R_{\infty} b}{\mu_0 I^{\text{tot}}}; \quad (111)$$

(2) we divided the sum of Equations ((77) and (78)) by a common factor, $\mu_0(I^{\text{tot}})^2R_\infty/r^4$; (3) we used Equations (2) and (5) to express the ∇_2 operator; and (4) we used Equation (32) to relate the total current to B_c , $\mu_0I^{\text{tot}} = 2B_cR_\infty$. However, we do not use the assumption of $p^{\text{tot}} = p^{\text{tot}}(\psi)$ any longer. To the contrary, while ψ is a function of u, p^{tot} is now assumed to be a function of both u and v.

For a thin current filament, i.e., for $\sinh u \gg 1$, the term that is proportional to $\sinh u$ is dominant in Equation (110) and the following simplifications are possible. First, by keeping only the n=0 term in the expansion given by Equation (A15), the geometric factor multiplying the strapping field becomes $(r/R_\infty)^{\frac{3}{2}} \approx \bar{Q}_{-\frac{1}{2}}^{-1}(u)/2\pi \approx \bar{Q}_{-\frac{1}{2}}^{-1}(u_0)/2\pi$. Second, the strapping field itself is approximated using Equations (94), (44), and (97):

$$\frac{B^{(s)}}{2B_c} = -\frac{L_0}{4\pi\mu_0 R_\infty} \approx -\frac{L_0^{(\text{ext})}}{4\pi\mu_0 R_\infty}
= -\frac{\pi}{8} \frac{\bar{P}_{-\frac{1}{2}}^{-1}(u_0)}{\bar{Q}_{-\frac{1}{2}}^{-1}(u_0)} = -\frac{\pi\tilde{\psi}(u_0)}{\bar{Q}_{-\frac{1}{2}}^{-1}(u_0)},$$
(112)

since for a thin filament the inductance of the external field dominates (see Figure 7). Third, we use Equation (41) to approximate the radial unit vector, $\mathbf{e}_r \approx -\sin v \, \mathbf{e}_v - \cos v \, \mathbf{e}_u$. With these approximations, one can rewrite Equation (110)

keeping only the leading terms in the factors multiplying e_{ν} , e_{μ} :

$$\left(\tilde{j}\frac{d\tilde{\psi}}{du} - \frac{\partial \tilde{p}^{\text{tot}}}{\partial u}\right) \mathbf{e}_{u} - \left(\frac{\partial \tilde{p}^{\text{tot}}}{\partial v} + \frac{\sin v}{\sinh u}\right) \times \left\{\frac{\tilde{j}[\tilde{\psi} - \tilde{\psi}(u_{0})] - \tilde{p}^{\text{tot}}}{2} + \frac{3\tilde{b}^{2}}{4} + \frac{7\tilde{p}}{2}\right\} \mathbf{e}_{v} = 0.$$
(113)

In the zeroth-order approximation for small $\frac{\sin v}{\sinh u}$, one gets $\partial \tilde{p}^{\text{tot}}/\partial v = 0$ and the condition for the coefficient of e_u to vanish results in the reduced GS equation (Equation (80)), giving:

$$\left(\frac{\tilde{b}^2}{2}\right)^{(0)} = \frac{1}{1+\beta} \int_{u_0}^{u} \tilde{j}(u_1) \frac{d\tilde{\psi}}{du_1} du_1,$$

$$\tilde{p}^{(0)} = \frac{\beta}{1+\beta} \int_{u_0}^{u} \tilde{j}(u_1) \frac{d\tilde{\psi}}{du_1} du_1,$$
(114)

where the superscript "(0)" denotes the zeroth-order approximation. To get the first-order approximation, Equations (114) are used to evaluate the expression in braces in Equation (113). Particularly, for uniform current form, $(\tilde{p}^{(\text{tot})})^{(0)} = \tilde{j} \ [\tilde{\psi} - \tilde{\psi}(u_0)]$, so that the first term inside the braces vanishes. In the first-order approximation, corrections that are $\propto \frac{\cos v}{\sinh u}$ should be added to the magnetic and gas-kinetic pressures, to get the factor multiplying e_v vanish:

$$\left(\frac{\tilde{b}^2}{2}\right)^{(1)} = \frac{1 + \frac{3}{2} \frac{\cos v}{\sinh u}}{1 + \beta} \int_{u_0}^{u} \tilde{j}(u_1) \frac{d\tilde{\psi}}{du_1} du_1,
\tilde{p}^{(1)} = \frac{\beta \left(1 + \frac{7}{2} \frac{\cos v}{\sinh u}\right)}{1 + \beta} \int_{u_0}^{u} \tilde{j}(u_1) \frac{d\tilde{\psi}}{du_1} du_1,$$
(115)

where, according to Equations (5) and (7),

$$\frac{\cos v}{\sinh u} = \frac{R^2 - R_{\infty}^2}{2rR_{\infty}}.$$
 (116)

The corrections given by Equations (115) and (116) have two remarkable properties. First, the corrections do not modify the integral E_0 in Equation (94), hence, the estimate for the strapping field. Indeed, E_0 reduces to integrals of $b^2(u, v)$ and p(u, v) over dudv; therefore, the contributions to the integrand, which are proportional to $\cos v$, vanish once integrated over dv.

Now, we use Equations (115) and (116) as well as Equations (85), (88), and (89) to derive the first-order approximation for the dimensional quantities:

$$B_{\varphi}^{(1)} = \sqrt{\frac{1 + \frac{3}{2} \frac{R^2 - R_{\infty}^2}{2rR_{\infty}}}{1 + \beta}} B_c \left(\frac{R_{\infty}}{r}\right)^{\frac{3}{2}} B^{(\text{tor})}(u),$$

$$P^{(1)} = \frac{\beta \left(1 + \frac{7}{2} \frac{R^2 - R_{\infty}^2}{2rR_{\infty}}\right)}{1 + \beta} \left(\frac{R_{\infty}}{r}\right)^3 \frac{[B_c B^{(\text{tor})}(u)]^2}{2u_0}.$$
(117)

We note that

$$B^{ ext{(tor)}} \propto \left[\int_{u_0}^u \tilde{j}\left(u_1\right) \frac{d\tilde{\psi}}{du_1} du_1
ight]^{\frac{1}{2}} \propto \left[\tilde{\psi}(u) - \tilde{\psi}(u_0)
ight]^{\frac{1}{2}}$$

for a uniform current form factor. Within the adopted accuracy, we can approximate $(R^2-R_\infty^2)/2rR_\infty\approx (r-R_\infty)/R_\infty$, so that $\left[1+\frac{3}{4}(R^2-R_\infty^2)/rR_\infty\right]^{\frac{1}{2}}\approx (r/R_\infty)^{\frac{3}{4}}$ and $1+\frac{7}{4}(R^2-R_\infty^2)/rR_\infty\approx (r/R_\infty)^{\frac{7}{2}}$. Finally, we arrive at the following scaling for the current function (see Section 5.1 for more detail): $rB_\varphi^{(1)}\approx {\rm const}\times r^{\frac{1}{4}}[\tilde\psi-\tilde\psi(u_0)]^{\frac{1}{2}}$ as well as for pressure: $P^{(1)}\approx {\rm const}\times r^{\frac{1}{2}}[\tilde\psi-\tilde\psi(u_0)]$. The second remarkable property of the first-order approximation is that these quantities only depend on the function, $r^{\frac{1}{2}}[\tilde\psi-\tilde\psi(u_0)]$, which can be expressed in terms of the total flux function, $\Psi^{\rm tot}=\Psi+B^{(\rm s)}r^2/2$, including the contribution from the uniform strapping field, as we demonstrate next.

To express the function, $r^{\frac{1}{2}}[\tilde{\psi}(u) - \tilde{\psi}(u_0)]$, that vanishes as $u \to u_0$, we redefine the total flux function by adding a constant, equal to $\frac{3}{2}B^{(s)}R_{\infty}^2$, so that as $u \to u_0$, the total flux function vanishes, $\tilde{\Psi}^{\text{tot}} \to 0$. Using Equations (32), (112), and (A16), the redefined flux function can be transformed as follows:

$$\Psi^{\text{tot}} = \Psi + B^{(s)} \left(\frac{1}{2} r^2 + \frac{3}{2} R_{\infty}^2 \right) = \mu_0 \sqrt{r R_{\infty}} I^{\text{tot}} \\
\times \left\{ \tilde{\psi} + \frac{B^{(s)}}{2B_c} \left[\frac{1}{2} \left(\frac{r}{R_{\infty}} \right)^{\frac{3}{2}} + \frac{3}{2} \left(\frac{R_{\infty}}{r} \right)^{\frac{1}{2}} \right] \right\} \\
\approx \mu_0 \sqrt{r R_{\infty}} I^{\text{tot}} \left[\tilde{\psi} - \frac{\pi \tilde{\psi}(u_0)}{\bar{Q}_{-\frac{1}{2}}^{-1}(u_0)} \frac{\bar{Q}_{-\frac{1}{2}}^{-1}(u)}{\pi} \right] \\
\approx (\mu_0 R_{\infty}^{\frac{1}{2}} I^{\text{tot}}) r^{\frac{1}{2}} [\tilde{\psi}(u) - \tilde{\psi}(u_0)]. \tag{118}$$

Thus, the pressure and current functions both depend on the function, $r^{\frac{1}{2}}[\tilde{\psi}(u)-\tilde{\psi}(u_0)]$, which differs only by a constant factor from the flux function, Ψ^{tot} . In order to eliminate the extra contributions to the force in Equation (110), which are aligned with \boldsymbol{e}_u and are proportional to $\cos v$, one needs to replace the $\tilde{j}^{(0)}=\tilde{j}_0(u)\approx \text{const}$ approximation of the current density with:

$$j^{(1)} = I^{\text{tot}} \tilde{j}_0(u) \left(1 + 2C_{\frac{3}{4}} \frac{\cos v}{\sinh u} \right)$$
$$\approx I^{\text{tot}} \tilde{j}_0(u) \left[1 + \left(\frac{3}{2} + \frac{2\beta}{\beta + 1} \right) \left(\frac{r}{R_{\infty}} - 1 \right) \right]. \tag{119}$$

This modification satisfies the exact Grad–Shafranov equation (Equation (66)), requiring that

$$J_{\varphi} = \frac{1}{r} \frac{d}{d\Psi} \frac{(rB_{\varphi})^2}{2\mu_0} + r \frac{dP}{d\Psi},\tag{120}$$

hence,

$$j^{(1)} = I^{\text{tot}} \frac{\tilde{j}_0(u)}{\beta + 1} \left[\left(\frac{r}{R_\infty} \right)^{\frac{3}{2}} + \beta \left(\frac{r}{R_\infty} \right)^{\frac{7}{2}} \right]. \tag{121}$$

This becomes Equation (119) for $|r-R_\infty| \ll R_\infty$. The extra current harmonics, $j_{\pm 1}\cos v = C_{\frac{3}{4}}I^{({\rm tot})}\frac{\tilde{j}_0(u)}{\sinh u}\cos v$, in Equation (119) result in: (1) the generation of the first harmonics of the reduced flux function, $\psi_{\pm 1}(u)\cos v \propto C_{\frac{3}{4}}$; (2) the modification of the external field given by

Equation (27); and (3) an extra requirement on the magnitude of the strapping field, which, in addition to the zeroth-order approximation of $\propto L^{(\text{ext})}t_0$ given by Equation (112), also gives a contribution of $\propto C_{\frac{3}{4}}$, in accordance with Equations (94) and (108). However, to satisfy the exact equilibrium condition, the strapping field must satisfy a more restrictive condition for not only its "average" magnitude, but also for the particular distribution over the current filament cross section (see details in Zakharov & Shafranov 1986, including the shapes of strapping field for different filament parameters), to separately balance the force on three current harmonics (for $n = 0, \pm 1$).

Based on these considerations, we arrive at an important conclusion. Although solving the reduced GS equation is sufficient to finding a configuration sufficiently close to equilibrium, this approach may look misaligned within the general framework of the full GS, since the current function and pressure are not directly expressed via the flux function. However, this contradiction is resolved with the improved approximation described here, since within the accuracy of the approximation, the functional dependencies become $rB_{\omega}^{(1)} \approx {\rm const} \times \sqrt{\Psi^{\rm tot}}$ and $P^{(1)} \approx {\rm const} \times \Psi^{\rm tot}$, in compliance with the full GS equation. Despite formally being more accurate and consistent, the improved equilibrium solution is more laborious and difficult to compute, and, which is even more problematic, poses more severe restriction on the shape of the strapping field. Specifically, three harmonic amplitudes, $\psi_{-1}^{(\text{ext})}, \psi_0^{(\text{ext})},$ and $\psi_1^{(\text{ext})}$ for the external field in Equations (28) and (29) should be prescribed. In a realistic magnetic field, which hardly satisfies these requirements, the "improved" solution can be even farther from equilibrium than the simple and easy-to-compute single-harmonic solution for n = 0. Solving the R-MHD equations with the simple n = 0 harmonic solution as the initial condition seems to be a more practical, and therefore preferred approach. This way, both the magnetic configuration and its external field automatically adjust to the realistic strapping field.

5.7. CME Generator Based on Finite β Zeroth Harmonic Solution

In actual numerical simulations of CMEs, an important distinction from idealized configurations is that only a part of the toroidal filament rises above the solar surface, with the center of configuration located at a depth, d, below the surface. From simple geometric considerations, one can determine the angular size of this circular arc above the solar surface:

$$\Delta \alpha = 2 \arccos \left(\frac{2R_{\odot}d - d^2 - R_{\infty}^2}{2(R_{\odot} - d)R_{\infty}} \right), \tag{122}$$

where R_{\odot} is the solar radius. For small values of d, the configuration gets close to an idealized situation when the highly conducting solar surface cuts the circular ring of the filament to two half circles. In this case, the "hidden" part of the filament (that is under the solar surface) can be considered as an "image" current below the surface. For such idealized situations, one gets $\Delta \alpha \approx \pi$. As long as in such a model the CME is driven by the hoop force, the work done by this force in the course of expansion (according to Equation (71)) can be expressed via the change in the total magnetic free energy, which, for the described circular arc, can be obtained from

Equation (108) as follows:

$$E_{\rm CME} = \frac{\Delta \alpha}{4\pi} (L_0^{\rm (ext)} + c_{\frac{3}{4}} \mu_0 R_{\infty}) (I^{\rm tot})^2.$$
 (123)

The mass of the ejecta is obtained from Equations (92), (103), and (107):

$$M_{\rm CME} = \frac{\Delta \alpha}{4\pi} \mu_0 R_{\infty} \frac{(I^{\rm tot})^2}{V_{A\varphi}^2},\tag{124}$$

where we assumed a low β plasma, so that $1+\beta\approx 1$, and the Alfvén speed inside the filament, $V_{A,\varphi}$, has been defined in Equation (91). Assuming that in the CME the available free energy is fully converted to the kinetic energy of ejecta, $E_{\rm CME}=\frac{1}{2}M_{\rm CME}V_{\rm CME}^2$, i.e., by neglecting the interaction of the strapping field with the starting to expand flux rope, we can estimate the asymptotic CME speed, which is independent of the current, $I^{\rm tot}$, and the angular extent of the erupting arc, $\Delta\alpha$:

$$V_{\rm CME} = \sqrt{2\left(\frac{L_0^{({\rm ext})}}{\mu_0 R_\infty} + c_{\frac{3}{4}}\right)} V_{{\rm A},\varphi} \sim 2V_{{\rm A},\varphi}.$$
 (125)

It can be seen that the normalized external inductance, $L_0^{(\rm ext)}/(\mu_0 R_\infty)$, controls the physically important speed ratio, $V_{\rm CME}/V_{A_\varphi}$. According to Equation (95), this inductance is a function of u_0 , but it also can be parameterized with κ_0' or with the a/R_0 ratio (see Figure 7). For a thin filament, this coefficient is about 1.2–2.5, indicating that the CME speed can exceed the Alfvén speed in the initial filament configuration by a factor of 2 (see Equation (125)). Another potentially important contribution to the energy budget is due to gravity. With an account of negative potential energy, the energy conservation law, $E_{\rm CME}-\frac{GM_\odot}{R_\odot}M_{\rm CME}=\frac{1}{2}M_{\rm CME}V_{\rm CME}^2$, gives:

$$V_{\rm CME}^2 = 2 \left(\frac{L_0^{(\rm ext)}}{\mu_0 R_{\infty}} + c_{\frac{3}{4}} \right) V_{\rm A,\varphi}^2 - V_G^2,$$
 (126)

where G is a gravitation constant, M_{\odot} is a solar mass, and

$$V_G = \sqrt{\frac{2GM_{\odot}}{R_{\odot}}} \approx 615 \,[\text{km/s}] \tag{127}$$

is an escape velocity.

The fact that our model can produce super-Alfvénic CMEs raises several interrelated questions, such as what is the mechanism of energy conversion from magnetic free energy to kinetic energy of the ejecta? How fast is the energy conversion?

Under these circumstances, an essential element of the CME initiation scenario is magnetic reconnection. In addition to fast removal of the field tying the current filament to the active region and subsequent acceleration of the CME to super-Alfvénic speeds, the reconnection can also explain the X-ray flare accompanying the CME (see, e.g., Forbes 2000), as well as the accelerated particle release (Masson et al. 2013).

This new scenario is demonstrated in Figure 8. Previously (see Section 5.3), we considered a uniform horizontal strapping field, which at the center of the current loop was oppositely oriented to the magnetic field of the current filament, $B_c \mathbf{n}_c$. However, the magnitude of this strapping field was smaller than B_c , and therefore, the superposed field, $(B_c + B^{(s)})\mathbf{n}_c$, did not change direction (see Figure 5 and compare it to the case of the no-strapping field, depicted in Figure 4). In contrast with the uniform field, the new scenario involves an altitude-

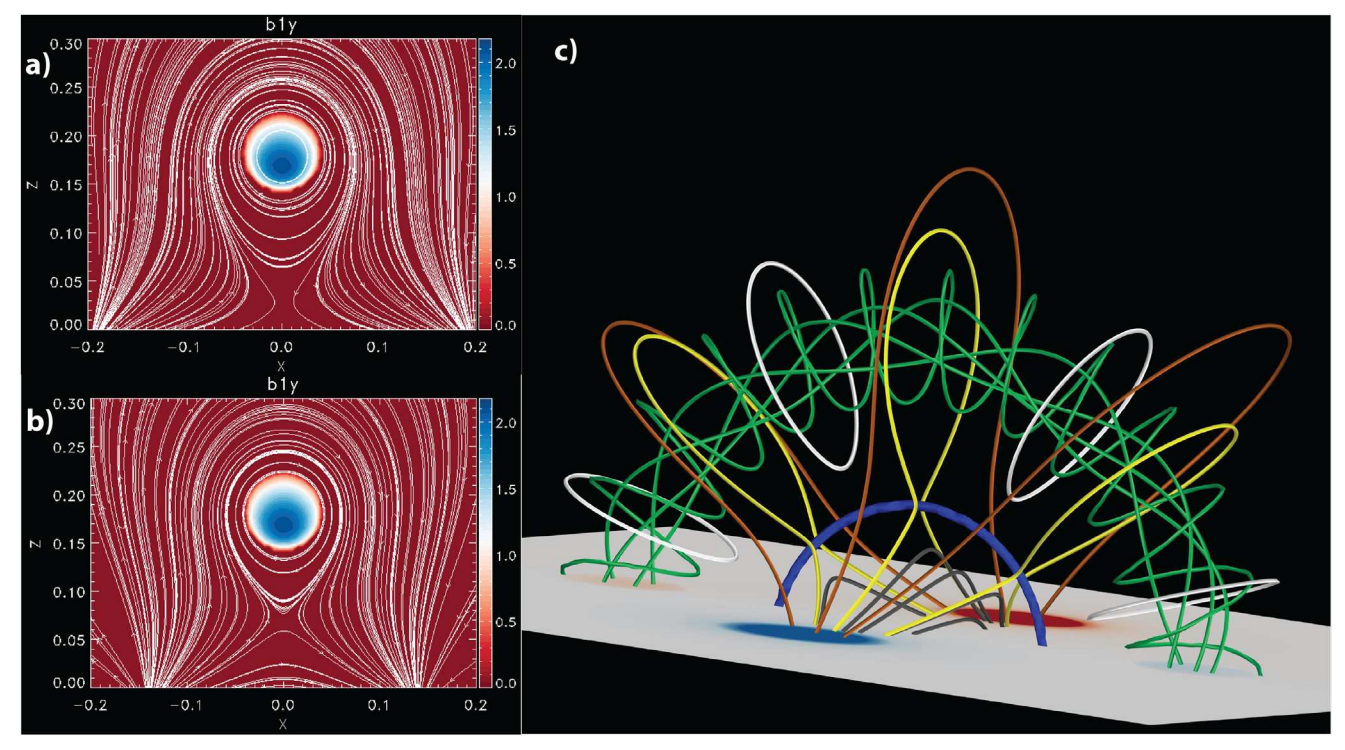


Figure 8. Magnetic field lines from the current filament characterized by $R_{\infty} = 0.2R_{\odot}$, $\kappa'_0 = 0.1$, $B_c = 1$, strapped by the field from a pair of positive and negative magnetic charges. The configuration center is at a depth of $d = 0.025R_{\odot}$ below the solar surface; the distance, 2D, between the charges is $D = R_{\infty}$ for panel (a) and $D = 0.7R_{\infty}$ for panels (b) and (c). Null points can be seen in panels (a) and (b), which show meridional cross sections of the configuration, similarly to Figures 4 and 5. In the 3D topology, shown in panel (c), the null line is marked with a thick blue line.

dependent overarching strapping field. This strapping field originates from the active region, and it is anchored to the solar surface. The strapping field balances the hoop force at the apex, and it can be sufficiently strong near the solar surface to flip the direction of the superposed field. This flip results in the formation of *null points* that are the seeds of future reconnection.

A still idealized, but more realistic, case of a strapping field created by a pair of positive and negative magnetic charges at the axis of symmetry of the configuration, which mimic positive and negative magnetic spots of a bipolar active region (see Titov & Démoulin 1999) is illustrated in Figure 8. On the left (panels (a) and (b)), we demonstrate how the field topology depends on the distance, 2D, between the charges. Here we used current filament parameters, $R_{\infty} = 0.2R_{\odot}$, $\kappa'_0 = 0.1$, B_c = 1, while the depth of the configuration center was $d = 0.025R_{\odot}$. The magnitude of the charges was chosen in a way that the field at the current filament location is sufficient for strapping. For $D \gg R_{\infty}$ (not shown) the strapping field is almost uniform, the only distinction from Figure 5 is that at large distances the field lines connect to the solar surface. In the intermediate case when $D = R_{\infty}$ (see Figure 8(a)), the field of the current filament near the solar surface is balanced by the strapping field; therefore, the null point forms near the origin. When the strapping field is even more nonuniform, $D = 0.7R_{\infty}$ (see Figure 8(b)) the null point raises and gets closer to the filament.

Figure 8(c) shows the 3D topology of the field for the $D=0.7R_{\infty}$ case. There are five families of topologically different magnetic field lines:

1. Twisted magnetic field lines inside the filament (green lines),

- 2. Circular field lines looping around the filament generated by its current (white circles),
- 3. Arcade-type strapping magnetic field lines originating from the magnetic charges (brown lines). Their tension balances the hoop force and maintains the equilibrium,
- 4. Below the null line (marked by blue) there are black lines connecting the positive and negative magnetic charges. These field lines are completely disconnected from the filament and its own field,
- 5. Stretched magnetic field lines with null points (yellow lines). These are separators: the upper loop separates the brown strapping field lines from the field lines looping around the filament. The bottom loop separates the strapping (brown) field lines from the black field lines closed below the null line.

Using numerical simulations for a nearly identical configuration, Roussev et al. (2003) demonstrated that reconnection at the null line naturally results in loss of equilibrium (note the similarity between our Figure 8(c) and Figure 1 in Roussev et al. 2003). This loss of equilibrium is due to the fact that the strapping field (brown lines) partially reconnects and its strapping effect decreases. Note that the strapping field is introduced to ensure equilibrium, while the height dependence of the realistic strapping field in the active region naturally results in the appearance of null points and null lines, which make the configuration prone to magnetic reconnection, thus potentially breaking the equilibrium.

It is important that when applying this methodology to realistic CME simulations, it is not enough to choose a location and appropriate model parameters to obtain an equilibrium configuration of the underlying active region together with the superposed filament model (as described by Titov et al. 2014).

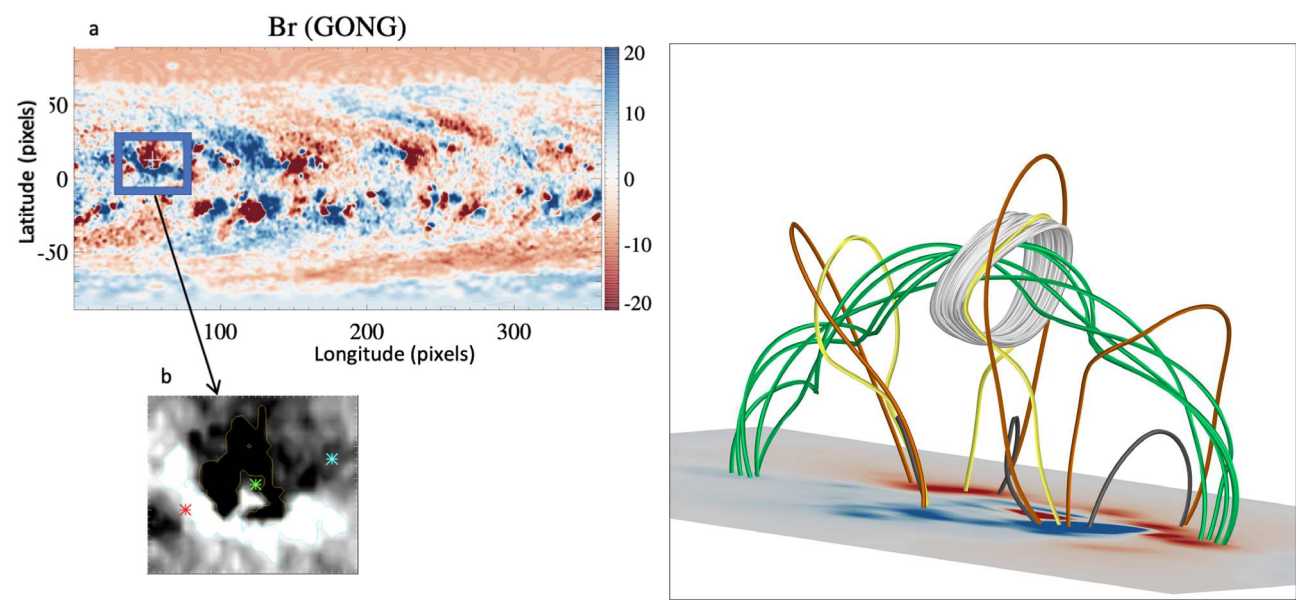


Figure 9. Top left: GONG magnetogram as of 2013 April 11 with intensified weak field. Bottom left: zoomed in AR field with the chosen locations for the current filament footpoints (red and blue asterisks) and the center of configuration (green asterisk). Right panel: the magnetic configuration superposed with realistic magnetic field of the active region adjusted to simulate the CME event of 2013 April 11.

In addition, one must find a configuration that is ripe for spontaneous eruption due to magnetic reconnection. Note that reconnection by itself does not have to be spontaneous (although it can be—see Roussev et al. 2003). Another possible mechanism to enforce reconnection is horizontal motion of photospheric plasma together with the frozen-in footpoints of strapping field lines converging toward the polarity inversion line, flux cancellation (see, e.g., Linker et al. 2003). Such motion builds up the current along the null loci below the flux rope ending up with reconnection and further eruption.

In Figure 9 we present such a configuration created to simulate the CME event of 2013 April 11. The GONG magnetogram as of 2013 April 11 is shown in the top-left panel. Because of the limitations of the observed geometry, there is significant uncertainty of the radial magnetic field measurements in the polar regions. In order to reduce this uncertainty and achieve better agreement of global simulation results with observations, it is customary to modify the photospheric radial magnetic field in the polar regions. Specifically, the observed radial field, $B_R^{(\text{obs})}$, used as the boundary condition at $R = R_{\odot}$, is intensified in weak field regions:

$$B_R|_{R=R_{\odot}} = \text{sign}(B_R^{\text{(obs)}})$$

 $\times \min(3.5|B_R^{\text{(obs)}}|,|B_R^{\text{(obs)}}|+5 \text{ Gs}).$ (128)

To get a 3D distribution of the strapping field, the Potential Field Source Surface Model (PFSSM) is applied by expressing the intensified field as a series of spherical harmonics to the order of 180.

Once the 3D PFSSM field of the active region and the approximate location of the CME source are obtained, we iterate the locations of the two filament footpoints near the polarity inversion line and analyze the PFSSM field along the filament passing through these footpoints and the topology of the total (superposed) field. The iterated locations are shown with red and blue asterisks in the bottom-left panel of Figure 9,

displaying a zoomed fragment of the magnetogram. The best choice for the center of configuration in heliographic coordinates are (80°, 13°) as shown with the green asterisk in the bottom-left panel of Figure 9) and the depth is $d=0.03R_{\odot}$. The major and minor radii of the current filament are $0.21R_{\odot}$ and $0.04R_{\odot}$, with the horizontal axis of symmetry rotated 290° counterclockwise from the local direction of heliographic parallel. The helicity sign is negative.

Under these conditions, the strapping field along the filament is approximately uniform and perpendicular to the plane of filament. The magnitude of the strapping field, $B^{(s)} \approx -2.7$ Gauss, determines the current according Equation (94), thus balancing the hoop force in equilibrium. On the other hand, the topology of superposed field of the current filament on top of the active region (presented in the right panel of Figure 9) shows null points below the filament, which make the configuration prone to reconnection, and thus eruption. As we described in this paper, one must chose the model parameters in a way that the resulting CME matches the total mass and kinetic energy of the observed eruption. With these choices, our proposed eruption generator will automatically match a significant number of observational constraints.

Note then when the described configuration is used as an initial condition for subsequent full MHD runs (similarly to the way as described by Török et al. 2018), the solution with $\beta = \text{const} > 0$ breaks an equilibrium due to imbalanced gravity. The variation of $\beta \propto \exp\left(-\frac{g_{\odot}m_ih}{k_B(T_e+T_i)}\right)$ (where $g_{\odot} = GM_{\odot}/R_{\odot}^2$), with altitude, h, can be introduced, which prevents the ejecta from falling down along the filament. The full force balance should also account for the component of gravity force directed toward the local curvature center of the filament, which partially balances the hoop force and, in effect, reduces the strapping field required for equilibrium. Here we omit these technical details, which are easy to derive from Equation (121) for the mass of the ejecta.

6. Discussion and Summary

In this paper we described the relations between the current, the poloidal field it produces, and the toroidal field preventing the pinch-effect by accurate analytical expressions that allow for finite thermal pressure. However, we only provide an integral approximation for the strapping field. This is still very useful, because in CME simulations, the strapping field is quite uncertain: it is nonuniform and even if we were able to describe an exact equilibrium of ideally shaped ring with the prescribed current would not describe a realistic scenario. On the other hand, the accurately described filament in which the pinch-effect is prevented is capable of self-adjusting its height and curvature radius to create an equilibrium configuration.

It is important that the direction of the strapping field is opposite to that of B_c , and its magnitude for thin filament (of large inductance and large stored magnetic free energy) can exceed the field at the axis.

In summary, this paper presents a mathematically rigorous extension of the Titov & Démoulin (1999) and Titov et al. (2014) CME generator based on the Grad & Rubin (1958)–Shafranov (1966) equation. The main new features of the proposed model are as follows:

- 1. The filament is filled with plasma; thus, the model describes a finite β initial configuration with finite mass and energy,
- The model describes an equilibrium solution that will spontaneously erupt due to magnetic reconnection of the strapping magnetic field arcade,
- 3. There are analytic expressions connecting the model parameters to the asymptotic velocity and total mass of the resulting CME, providing a way to connect the simulated CME properties to multipoint coronograph observations.

Acknowledgments

We are grateful to Drs. V. S. Titov, J. Linker, J. Karpen, and S. Antiochos for useful discussions and to Dr. Lulu Zhao for her kind help in visualization. This work was supported by a NASA LWS Strategic Capability (SCEPTER) project at the University of Michigan under NASA grant 80NSSC22K0892, and by NSF ANSWERS grant GEO-2149771.

Appendix Toroidal Functions

A.1. Definition and Expressions via Hypergeometric Functions

The toroidal functions (see definition in Bateman & Erdélyi 1953) used in the present paper are

$$\begin{split} \bar{Q}_{n-\frac{1}{2}}^{-m}(u) &= \sqrt{2 \sinh u} \ Q_{n-\frac{1}{2}}^{-m}(\cosh u), \\ \bar{P}_{n-\frac{1}{2}}^{-m}(u) &= \sqrt{2 \sinh u} \ P_{n-\frac{1}{2}}^{-m}(\cosh u), \quad m = 0, 1. \end{split}$$
 (A1)

They differ from the usually introduced associated Legendre functions of semi-integer index, $Q_{n-\frac{1}{2}}^{-m}(\cosh u)$, $P_{n-\frac{1}{2}}^{-m}(\cosh u)$,

by a factor of $\sqrt{2 \sinh u}$. The associated Legendre function of the first kind is expressed in terms of the hypergeometric series, $F(a, b; c; z) = {}_{2}F_{1}(a, b; c; z)$ (see Equation (8).852(2) in Gradshteyn & Ryzhik (2014) and also Equation (5) in Bateman

& Erdélyi 1953):

$$\bar{P}_{n-\frac{1}{2}}^{-1}(u) = \frac{\kappa^3}{4} (\kappa')^n F\left(\frac{3}{2}, n + \frac{3}{2}; 3; \kappa^2\right). \tag{A2}$$

According to Equation (8.752(3)) in Gradshteyn & Ryzhik (2014), $P_{\nu}^{-1}(\cosh u) = \frac{1}{\sinh u} \int_{1}^{\cosh u} P_{\nu}(z) dz$, so that:

$$\frac{d}{du}[\bar{P}_{n-\frac{1}{2}}^{-1}(u)] = \bar{P}_{n-\frac{1}{2}}(u) - \frac{2-\kappa^2}{2\kappa^2}\bar{P}_{n-\frac{1}{2}}^{-1}(u)$$
 (A3)

where

$$\bar{P}_{n-\frac{1}{2}}(u) = \kappa(\kappa')^n F\left(\frac{1}{2}, n + \frac{1}{2}; 1; \kappa^2\right).$$
 (A4)

In the particular case of n = 0, the difference of the two functions in Equation (A3) can be expressed through a single toroidal function (see Bateman & Erdélyi 1953, Equation (8)):

$$\frac{d}{du}[\bar{P}_{-\frac{1}{2}}^{-1}(u)] = \frac{3\kappa'}{\kappa^2} \bar{P}_{\frac{1}{2}}^{-1}(u). \tag{A5}$$

For $\kappa \approx 1$ the original hypergeometric series in Equation (A2) converges slowly, and it is worthwhile to transform the series to one based on the variable, $1 - \kappa^2$ (see Equations (15.1.2), (15.8.10), and (15.8.12) in DLMF 2021). Specifically, at $\kappa' \to 0$, one gets

$$\bar{P}_{-\frac{1}{2}}^{-1}(u) \approx \frac{4}{\pi} \left(\log \frac{4}{\kappa'} - 2 \right), \qquad \bar{P}_{\frac{1}{2}}^{-1}(u) \approx \frac{4}{3\pi\kappa'}.$$
 (A6)

The toroidal function of the second kind is given by Equations (8.736(4)) and (8.852(1)) in Gradshteyn & Ryzhik (2014):

$$\bar{Q}_{n-\frac{1}{2}}^{-1}(u) = -\frac{\Gamma(n-\frac{1}{2})\sqrt{\pi}}{\Gamma(n+1)}\kappa^{3}(\kappa')^{n}F$$

$$\times \left(\frac{3}{2}, n+\frac{3}{2}; n+1; (\kappa')^{2}\right)$$
(A7)

According to Equation (8).752(5) in Gradshteyn & Ryzhik (2014), $Q_{\nu}^{-1}(\cosh u)=-\frac{1}{\sinh u}\int_{\cosh u}^{\infty}Q_{\nu}(z)dz$, and

$$\frac{d}{du}[\bar{Q}_{n-\frac{1}{2}}^{-1}(u)] = \bar{Q}_{n-\frac{1}{2}}(u) - \frac{2-\kappa^2}{2\kappa^2}\bar{Q}_{n-\frac{1}{2}}^{-1}(u)$$
 (A8)

where (see Equation (8).852 in Gradshteyn & Ryzhik 2014):

$$\bar{Q}_{n-\frac{1}{2}}(u) = \frac{\Gamma(n+\frac{1}{2})\sqrt{\pi}}{\Gamma(n+1)}\kappa(\kappa')^{n}$$

$$\times F\left(\frac{1}{2}, n+\frac{1}{2}; n+1; (\kappa')^{2}\right) \tag{A9}$$

In the particular case of n = 0, Equation (A8) reduces to a small difference of two separate hypergeometric functions, are which both near unity. A more practical way to calculate this is to express in Equation (A8) via a single function using Equation (8).734(2) in Gradshteyn & Ryzhik (2014):

$$\frac{d}{du}[\bar{Q}_{-\frac{1}{2}}^{-1}(u)] = \frac{3\kappa'}{\kappa^2}\bar{Q}_{\frac{1}{2}}^{-1}(u)$$

$$= -3\pi\kappa(\kappa')^2 F\left(\frac{3}{2}, \frac{5}{2}; 2; (\kappa')^2\right). \tag{A10}$$

For $\kappa' \to 0$, one gets

$$\begin{split} \bar{Q}_{-\frac{1}{2}}^{-1}(u) &\approx 2\pi, \quad \bar{Q}_{\frac{1}{2}}^{-1}(u) \approx -\pi\kappa', \quad \frac{d}{du}[\bar{Q}_{-\frac{1}{2}}^{-1}(u)] \\ &\approx -3\pi(\kappa')^2, \quad \frac{d}{du}[\bar{Q}_{\frac{1}{2}}^{-1}(u)] \approx \pi\kappa' \approx -\bar{Q}_{\frac{1}{2}}^{-1}(u). \quad (A11) \end{split}$$

A.2. Wronskian of Toroidal Functions

The Wronskian of the Legendre functions may be found in Bateman & Erdélyi (1953), Equation (13):

$$\bar{Q}_{n-\frac{1}{2}}^{-1}(u)\frac{d\bar{P}_{n-\frac{1}{2}}^{-1}(u)}{du} - \bar{P}_{n-\frac{1}{2}}^{-1}(u)\frac{d\bar{Q}_{n-\frac{1}{2}}^{-1}(u)}{du} = \frac{2}{\left(\frac{1}{4} - n^2\right)}.$$
(A12)

A.3. Series of Toroidal Functions

series for semi-integer The Fourier powers $r/R_{\infty} = \sinh u/(\cosh u - \cos v)$ can be obtained from the following equation (see Shushkevich 1997):

$$\frac{1}{\sqrt{2(\cosh u - \cos v)}} = \frac{1}{\pi} \sum_{n = -\infty}^{\infty} Q_{n - \frac{1}{2}}(\cosh u) e^{inv}.$$
 (A13)

Equation (A13) $(\cosh u - \cos v)\sqrt{2/\sinh u}$, its LHS equals $\sqrt{R_0/r}$. On the RHS, one can express $\cos v = \frac{1}{2}(e^{inv} + e^{-inv})$ and partial sum of the multipliers by $e^{i\,nv}$ using Equations (8.734(3–4)) in Gradshteyn & Ryzhik (2014) reduces to $\frac{1}{2\pi}\bar{Q}_{n-\frac{1}{2}}^{-1}(u)$. Therefore:

$$\sqrt{\frac{R_{\infty}}{r}} = \frac{1}{2\pi} \sum_{n=-\infty}^{\infty} \bar{Q}_{n-\frac{1}{2}}^{-1}(u) e^{inv}.$$
 (A14)

Another series can be obtained by differentiating Equation (A13) over u and using Equations (8.736(4) and 8.752(4)) in Gradshteyn & Ryzhik (2014), which show that $dQ_{n-\frac{1}{2}}(\cosh u)/du = \left(n^2 - \frac{1}{4}\right)Q_{n-\frac{1}{2}}^{-1}(\cosh u)$:

$$\left(\frac{r}{R_{\infty}}\right)^{\frac{3}{2}} = \frac{2}{\pi} \sum_{n=-\infty}^{\infty} \left(\frac{1}{4} - n^2\right) \bar{\mathcal{Q}}_{n-\frac{1}{2}}^{-1}(u) e^{inv}. \tag{A15}$$

A particular linear combination of Equations (A14) and (A15) has the following remarkable property:

$$\frac{3}{2}\sqrt{\frac{R_{\infty}}{r}} + \frac{1}{2}\left(\frac{r}{R_{\infty}}\right)^{\frac{3}{2}} = \frac{1}{\pi}\sum_{n=-\infty}^{\infty} (1 - n^2)
\times \bar{Q}_{n-\frac{1}{2}}^{-1}(u)e^{inv} = \frac{1}{\pi}\bar{Q}_{-\frac{1}{2}}^{-1}(u) + O[(\kappa')^2], \tag{A16}$$

since the terms for $n = \pm 1$ vanish.

A.4. Some Integrals of the Modified Toroidal Functions

The current form factor functions, $j_n^{(m)}(u)$, utilized in this paper to approximate the profile of the toroidal current, are eigenfunctions of the equation,

$$\left[\sinh^2 u \left(-\frac{d^2}{du^2} + n^2\right) + \frac{3}{4}\right] j_n^{(m)} = E^{(m)} j_n^{(m)}. \tag{A17}\right]$$

While $\bar{Q}_{n-\frac{1}{2}}^{-1}(\cosh u)$ is the eigenfunction for E=0, we note that $\bar{Q}_{n-\frac{1}{2}}^{m+\frac{1}{2}}(\cosh u)$ is the eigenfunction for the eigenvalue of $E^{(m)} = 1 - \left(m + \frac{1}{2}\right)^2$. These eigenfunctions can be transformed to Legendre polynomials of argument coth u using Equation (8.739) in Gradshteyn & Ryzhik (2014). For the particular case of n = 0, we introduce the following definition (the subscript "0" denoting the n = 0 harmonic is omitted herewith):

$$j^{(m)}(u) = j_{\infty}^{(m)} P_m(\coth u),$$

where

$$j_{\infty}^{(m)}=\lim_{u\longrightarrow\infty}j^{(m)}(u).$$
 cifically,
$$j^{(0)}(u)\equiv i_{0\infty}^{(0)},\qquad E^{(0)}=\tfrac{3}{4},$$

 $j^{(1)}(u) = i_{0\infty}^{(1)} \coth u, E^{(1)} = -\frac{5}{4}$

For such current profiles, Equation (19) can be integrated analytically. Upon integrating by parts and using the equation $\left[-\frac{d^2}{du^2} + \frac{3}{4\sinh^2 u} \right] \bar{Q}_{-\frac{1}{2}}^{-1}(u) = 0, \text{ we get the following expression}$ for n = 0:

$$I(u) = \int_{u}^{\infty} \frac{j^{(m)}(u_{1})\bar{Q}_{-\frac{1}{2}}^{-1}(u_{1})du_{1}}{\sinh^{2}u_{1}} = \int_{u}^{\infty} \bar{Q}_{-\frac{1}{2}}^{-1}(u_{1})$$

$$\times \left[-\frac{d^{2}}{du_{1}^{2}} + \frac{3}{4\sinh^{2}u_{1}} \right] \frac{j^{(m)}(u_{1})}{E^{(m)}} du_{1}$$

$$= \frac{1}{E^{(m)}} \left[\frac{dj^{(m)}(u)}{du} \bar{Q}_{-\frac{1}{2}}^{-1}(u) - j^{(m)}(u) \frac{d\bar{Q}_{-\frac{1}{2}}^{-1}(u)}{du} \right]. \quad (A18)$$

ORCID iDs

Igor V. Sokolov https://orcid.org/0000-0002-6118-0469 Tamas I Gombosi https://orcid.org/0000-0001-9360-4951

References

Bateman, H., & Erdélyi, A. 1953, Higher Transcendental Functions, Vol. 1 (New York: McGraw-Hill)

Borovikov, D., Sokolov, I. V., Manchester, W. B., Jin, M., & Gombosi, T. I. 2017, JGRA, 122, 7979

DLMF 2017, NIST Digital Library of Mathematical Functions, Release 1.1.3 of 2021-09-15. http://dlmf.nist.gov/

Faddeev, L., Freyhult, L., Niemi, A. J., & Rajan, P. 2002, JPhA, 35, L133

Forbes, T. G. 2000, JGR, 105, 23153

Gibson, S. E., & Low, B. C. 1998, ApJ, 493, 460

Grad, H., & Rubin, H. 1958, in Proc. II UN Conf. on the Peaceful Uses of Atomic Energy, Vol. 31, Theoretical and Experimental Aspects of Controlled Nuclear Fusion, 190

Gradshteyn, I. S., & Ryzhik, I. M. 2014, Table of Integrals, Series, and Products (8th ed.; New York: Academic Press)

Jackson, J. D. 1999, Classical Electrodynamics (3rd ed.; New York, NY: Wiley) http://cdsweb.cern.ch/record/490457

Jin, M., Manchester, W. B., van der Holst, B., et al. 2013, ApJ, 773, 50

Jin, M., Manchester, W. B., van der Holst, B., et al. 2017, ApJ, 834, 172

Kliem, B., & Török, T. 2006, PhRvL, 96, 255002

Landau, L., & Lifshitz, E. 1984, in Course of Theoretical Physics, Vol. 8, Electrodynamics of Continuous Media, ed. L. Landau & E. Lifsitz (2nd ed.; Amsterdam: Pergamon), 225

Linker, J., Török, T., Downs, C., et al. 2016, in AIP Conf. Ser. 1720, SOLAR WIND 14: Proc. Fourteenth Int. Solar Wind Conf. (Melville, NY: AIP), 020002

Linker, J. A., Mikic, Z., Lionello, R., et al. 2003, PhPl, 10, 1971

Manchester, W. B., IV, van der Holst, B., Tóth, G., & Gombosi, T. I. 2012, ApJ, 756, 81

Manchester, W. B., IV, Vourlidas, A., Tóth, G., et al. 2008, ApJ, 684, 1448 Masson, S., Antiochos, S. K., & DeVore, C. R. 2013, ApJ, 771, 82

Morse, P., & Feshbach, H. 1953, Methods of Theoretical Physics, Part I (New York: McGraw-Hill)

Roussev, I. I., Forbes, T. G., Gombosi, T. I., et al. 2003, ApJL, 588, L45

Roussev, I. I., & Sokolov, I. V. 2006, GMS, 165, 89

Roussev, I. I., Sokolov, I. V., Forbes, T. G., et al. 2004, ApJL, 605, L73

Shafranov, V. D. 1966, in Reviews of Plasma Physics, ed. M. A. Leontovich, Vol. 2 (New York: Consultants Bureau), 103

Shushkevich, G. C. 1997, JTePh, 42, 436

Titov, V. S., & Démoulin, P. 1999, A&A, 351, 707

Titov, V. S., Downs, C., Török, T., et al. 2021, ApJS, 255, 9

Titov, V. S., Downs, C., Török, T., & Linker, J. A. 2022, ApJ, 936, 121

Titov, V. S., Török, T., Mikic, Z., & Linker, J. A. 2014, ApJ, 790, 163

Török, T., Downs, C., Linker, J. A., et al. 2018, ApJ, 856, 75

Yee, J., & Bellan, P. M. 2000, PhPl, 7, 3625

Zakharov, L. E., & Shafranov, V. D. 1986, in Reviews of Plasma Physics, ed.

M. A. Leontovich, Vol. 11 (New York: Consultants Bureau), 153